RESEARCH ARTICLE | DECEMBER 10 2025

Steady-state rotational dynamics of a weakly ionized hydrogen plasma under cross-field configuration

H. A. Muir ; N. Eschbach ; G. Rodway-Gant ; I. Vankov ; A. Chen ; B. Wrixon ; Z. Li ; A. Gunn ; G. Gregori

Phys. Plasmas 32, 123505 (2025)
https://doi.org/10.1063/5.0285228

Steady-state rotational dynamics of a weakly ionized hydrogen plasma under cross-field configuration

Cite as: Phys. Plasmas **32**, 123505 (2025); doi: 10.1063/5.0285228
Submitted: 13 June 2025 · Accepted: 13 November 2025 ·
Published Online: 10 December 2025

H. A. Muir,[1,a)] N. Eschbach,[1] G. Rodway-Gant,[1,2] I. Vankov,[1] A. Chen,[1] B. Wrixon,[1] Z. Li,[1] A. Gunn,[1] and G. Gregori[1,3]

AFFILIATIONS

[1]Alpha Ring International Limited, 5 Harris Ct Building B, Monterey, California 93940, USA
[2]Cavendish Laboratory, Department of Physics, University of Cambridge, JJ Thomson Ave., Cambridge CB3 0US, United Kingdom
[3]Department of Physics, University of Oxford, Parks Rd., Oxford OX1 3PU, United Kingdom

[a)]**Author to whom correspondence should be addressed:** heathermuir@alpharing.com

ABSTRACT

We study a novel device for generating a high-speed rotating plasma. The device weakly ionizes and accelerates a hydrogen gas in a co-axial cylindrical chamber via the perpendicular configuration of electrodes with a magnetic field generated by a superconducting magnet. It has been hypothesized that extreme velocities and plasma particle compression could be achieved under this configuration [Wong *et al.*, Phys. Plasmas **31**, 013101 (2024)]. This work develops a rigorous theoretical model of the bulk plasma dynamics under steady-state centrifugal operation. By exploiting the axisymmetry of the system and from the application of problem-specific governing assumptions, a steady-state 1D model for the rotational dynamics of the bulk plasma is derived. From here, we present fully analytical solutions for the radial profiles of the MHD model: (azimuthal velocity, particle densities, pressure) and a semi-analytical solution for the electric potential. Tables of self-consistent plasma parameters are computed to provide a comprehensive characterization of the bulk plasma state. The model can determine the peak velocities and plasma compression, and permits parametric studies to elucidate the complex and nonlinear relationships between operational device settings and the achieved steady-state plasma state condition. The new theoretical solutions, therefore, provide necessary insights into the viability of the novel device for high-energy-density plasma applications.

I. INTRODUCTION

It is proposed that gases can be accelerated to high rotational speeds via electromagnetic forcing, by utilizing the inherent electrical conductivity of a weakly ionized plasma. The Lorentz force, generated through carefully imposed perpendicular electric and magnetic fields, acts directly on charged particles. Collective motion of both charged and neutral species is realized via the collisional momentum exchange characteristic of a weakly ionized plasma. Electromagnetic fluid acceleration techniques are expected to realize significantly greater rotation velocities and system efficiencies compared to conventional methods, which remain limited by mechanical rotating components. Under this mechanism, substantial centrifugal compression is expected to be achieved, enabling innovative applications in high-energy, high-density plasma physics.

The concept of ($\mathbf{E} \times \mathbf{B}$)-driven plasma rotation has been extensively studied in the scientific literature[2–7] with relevance to numerous applications, including Hall thrusters,[8] Penning discharges,[9] and plasma centrifuges. Historically, centrifugal configurations were developed primarily for isotope separation[10–12] in low-throughput environments, utilizing the differential response of various species to separate isotopes and elements. Contemporary applications have expanded to include nuclear waste cleanup[13] and materials recycling,[14] necessitating enhanced throughput capabilities. Additionally, these rotating systems have been investigated for thermonuclear fusion applications.[15–18]

A critical aspect of such systems is the method used to establish the perpendicular electric field. The technique for applying bias voltage significantly influences device performance and distinguishes various plasma centrifuge approaches. Precise field control proves especially

crucial for mass separation applications.[7] Most implementations feature cylindrical geometry, producing a plasma column along an axis of symmetry. These devices generally employ solenoid-like magnetic configurations with uniform axial fields, and feature azimuthally symmetric electrode architectures that may be operated in either pulsed modes powered by capacitor bank discharges or steady-state modes using DC power supplies.

Several electrode configurations exist for imposing the required electric field. Common designs incorporate either cylindrical or ring-like electrodes at the outer diameter, coupled with smaller diameter biasing elements. Two principal approaches predominate: end biasing, which utilizes electrodes at the axial column extremities[3,19,20] or concentric rings allowing radial potential control;[12] and central biasing,[21–23] which employs an internal electrode within the plasma column. It is important to note that magnetic field lines often serve as isopotential surfaces under certain plasma conditions,[12] which is particularly relevant for configurations where multiple electrodes at the ends are used to shape electric field profiles. In schemes where the potential profile is not externally imposed, it is a self-organized result of the plasma behavior in that environment. This effect can significantly influence the overall potential structure and must be carefully considered when designing electrode arrangements for optimal plasma parameters and rotation characteristics.

The present work examines a device employing central biasing, in which a disk-shaped anode situated within a cylindrical hollow cathode creates a plasma column in the intervening gap. This arrangement, while similar to other coaxial configurations, differs in that the anode length is substantially shorter than the cathode. Rather than mass separation, this implementation focuses on bulk plasma rotation and compression for potential applications in generating conditions which have been proposed to be conducive to a novel method of fusion research.[24]

This rotational plasma device was the subject of a previously published numerical study[1] which considered a highly idealized, inviscid plasma system and aimed to elucidate the fundamental dynamics and assess the feasibility of the acceleration mechanism to compress the plasma. While this study produced qualitative and conceptual insights about the device function, these insights must be substantially built upon to provide quantitative estimates of the parameters that are critical to viability as a fusion plasma confinement method. This work therefore extends considerably upon the previous study by developing a realistic governing model for the weakly ionized hydrogen plasma which fills the cylindrical annular space. The model considers dissipative losses due to fluid viscosity, includes a thermodynamically consistent ionization model, as well as a critical review of anisotropic electrical conductivity for the plasma species present. Importantly, the model includes a formalized treatment of the electric potential field, based on the known experimental geometry and operational conditions. As the dissipative terms balance the Lorentz force driving terms, a new self-consistent theoretical model is presented for the steady-state plasma dynamics.

Via theoretical treatment of the coupled 1D equations of the governing model, analytical solutions have been developed for the azimuthal velocity profile of the plasma, as well as the plasma particle density. The solution for electric potential is somewhat more complex due to its dependence on several spatially varying parameters in the governing equations, and so its solution is treated analytically as far as possible, with the final step conducted via a numerical integration. From the density field, we can compute the compression ratio of the plasma at the outer boundary relative to the inner boundary. The model is applied to study a range of operating conditions in order to understand the complex relationship between system inputs and resultant plasma dynamics. The study reveals new fundamental insights about steady-state plasma profiles and how conditions may be optimized for confinement applications.

A. Rotational chamber device and experiments

The concepts explored in this paper relate to a real experimental device, with which laboratory experiments have been conducted and are ongoing. The rotation chamber is shown in Fig. 1 and consists of two coaxial cylinders with a positively biased center electrode and a grounded outer wall. The core of the system under study is illustrated in Fig. 2.

A DC voltage is applied across the annular space, establishing a DC discharge through the plasma. In this process, free electrons are accelerated by the electric field, colliding with neutral gas molecules and initiating impact ionization. This mechanism cascades to generate additional charged particles, which ultimately establishes a weakly ionized plasma, which carries and sustains a radial plasma current. A superconducting magnet is used to generate an axial magnetic field that is perpendicular to the radial electric field, leading to Lorentz forcing effects that drive charged particles to rotate azimuthally. The weakly ionized hydrogen contains a much higher proportion of neutrals than ions, with ionization degree expected on the order of 10^{-3}–10^{-6}. The neutral dominance within the weakly ionized plasma is thought to enhance the stability properties of the gas.[25] Fast-camera spectroscopy with ion-(442 nm) and neutral-(518 nm) filtered images showed co-rotating rings whose radial expansion sizes matched within a few percent at 3 Torr Ar,[1] which indicates the strong coupling of neutrals and ions due to frequent collisions.

The experiment is typically operated with a prefill hydrogen gas pressure of 3 Torr. Power is delivered by a DC power supply with a voltage limit of 800 V and a current limit of ∼20 A in constant current mode, though occasionally a capacitor bank is used for pulsed operation. Operational current levels that would force the power supply to operate at its maximum voltage or power limits are generally avoided. This approach ensures that the operational bias voltage—and consequently, the potential drop across the experiment and the resulting potential profile—is determined solely by the plasma arrangement rather than constrained by power supply limitations.

The operational mode of the plasma, referring to its general morphology, can take varying forms in this configuration. The mode depends on numerous input parameters, including geometry, cathode/anode material, and condition during operation, as well as magnetic field strength, pressure, inventory species, and current setting. The symmetry of the environment can also play a substantial role in determining the operational mode. Two primary modes are commonly observed: classic "spoke" discharges as described in Ref. 22, where a single spoke may rotate azimuthally or remain stationary (if the plasma arc forms via connection to some asymmetry or protrusion); and a "disk" mode, characterized by stable, diffuse, and azimuthally symmetric plasma. This paper specifically addresses the latter mode of operation observed in our experiments and shown in Fig. 3, where the experimental parameters are most commonly tuned to achieve this regime.

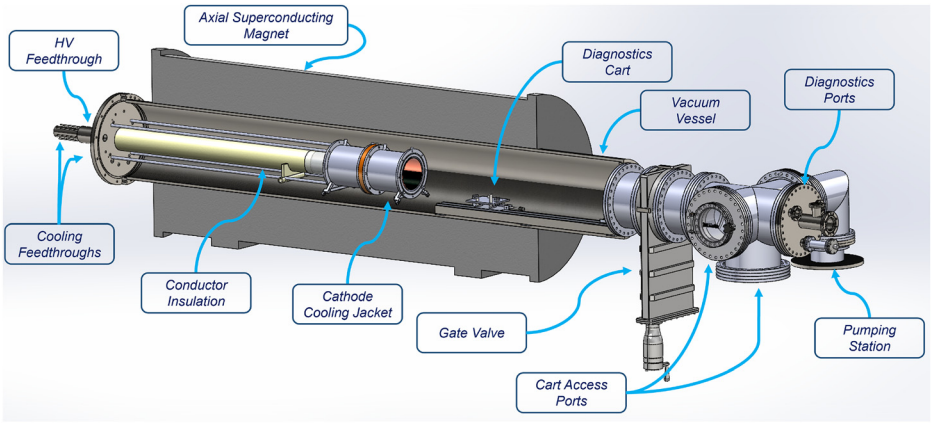

(a) Full experimental diagram

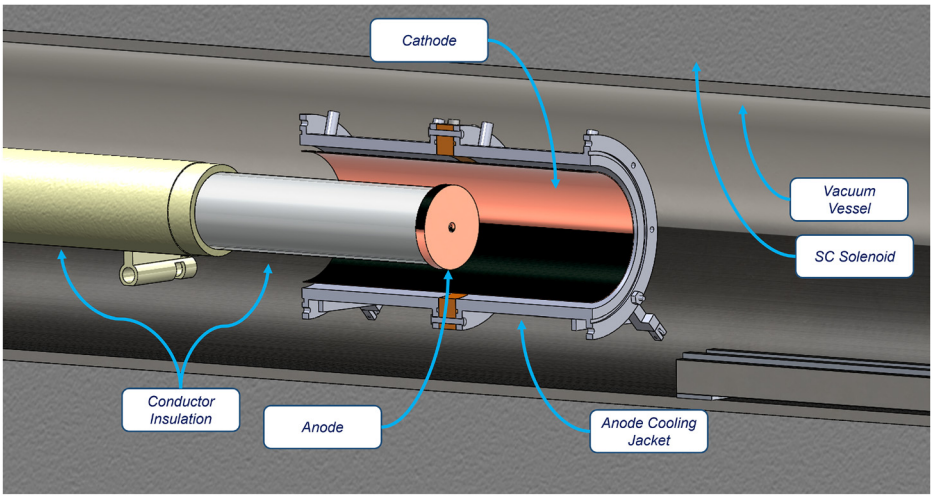

(b) Discharge volume diagram

FIG. 1. Partial cross-sectional engineering diagram of centrifuge experimental setup showing discharge volume configuration and electrode architecture.

II. THEORETICAL FORMULATION

The governing assumptions are stated *a priori* on the basis of experimental observations, physical reasoning, and prior literature. Each assumption is then verified *a posteriori* (using the plasma parameters computed) to ensure complete self-consistency (see Sec. II C); we cite the confirming magnitudes and outcomes when presenting the assumptions.

A. Governing assumptions

We are dealing with a weakly ionized hydrogen plasma with a temperature on the order of 1 eV and an ionization fraction within the range of 10^{-6}–10^{-3}. Since the plasma Debye length, as well as charged species gyration radii, are significantly smaller than the system characteristic length scale (L_0—taken to be the radial gap of the annular space), and inverse electron plasma frequency much smaller than the system characteristic timescale (τ_{sys}—taken to be the system's minimum bulk rotational period), the MHD equations appropriately govern. Accordingly, we treat the bulk plasma as quasi-neutral, $n_e \approx Zn_i$.

The regime under study is a highly collisional plasma, dominated by ion–neutral interactions that dictate momentum transfer and energy exchange. Magnetic induction and diffusion effects are decoupled in this regime, and therefore, the magnetic field is treated as static and imposed, confirmed by the calculation of a magnetic Reynolds number: $Re_m \ll 1$.

Analysis of dissociation under the experimental conditions (presented in Sec. II E) shows the plasma is formed from atomic hydrogen rather than diatomic molecules. From the dissociation and ionization analysis, we assess that we are operating with a $H/H^+/e^-$ plasma and the ionization fraction (χ_i) is calculated via the Saha ionization model. The negligible mass differential between ions (H^+) and neutrals (H) implies that even under very strong centrifugal forces, negligible radial mass separation occurs between ions and neutrals.

Regarding the ion–neutral momentum coupling: detailed analysis in Sec. II C shows the conditions $\nu_{in}\tau_{sys} \gg 1$, and $\lambda_{in}/L_0 \ll 1$ are satisfied, where ν_{in} is the ion–neutral collisional frequency, and λ_{in} is the ion–neutral mean free path (MFP). This collisional analysis indicates very strong ion–neutral coupling, which is consistent with the

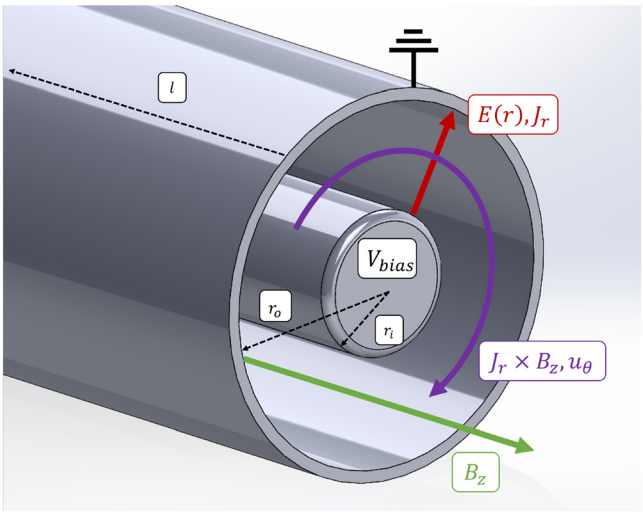

FIG. 2. Schematic of the anode–cathode system, depicting geometry of the annular space, and alignment of the electric cross magnetic fields, within which the plasma rotates.

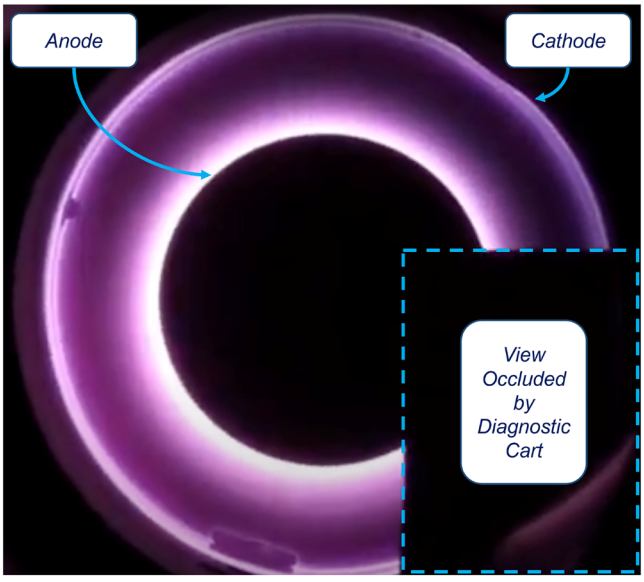

FIG. 3. Visible light camera image taken during experiments of the stable and diffuse plasma mode which forms and persists.

aforementioned experimental observations, as well as the previous numerical study, which showed very rapid coupling of the ion and neutral velocity profiles.[1] Since ions and neutrals are very tightly co-moving, ambipolar diffusion is negligible.

We extend the collisional analysis in Sec. II C to assess local thermal equilibration (LTE). First, we compare mean free paths for the species pairs, finding λ_{en}, λ_{in}, $\lambda_{ee} \ll L_0$, while $\lambda_{ie} > L_0$ (Table VI), which confirms frequent momentum-transfer collisions between all species pairs, except the rarer ion–electron collision. Second, we evaluate energy relaxation times $t^{(E)}$ relative to the dynamical time τ_{sys}. Although each elastic e–n collision transfers only $\mathcal{O}(2m_e/m_n)$ of electron energy, the high collision rate gives $t_{en}^{(E)} \ll \tau_{\text{sys}}$, i–n collisions (including resonant charge exchange) yield even faster heavy-particle equilibration, $t_{in}^{(E)} \ll \tau_{\text{sys}}$, and e–e collisions rapidly Maxwellize the electron distribution, $t_{ee}^{(E)} \ll \tau_{\text{sys}}$. While Coulomb e–i equilibration is found to have longer MFP and to be comparatively slow, the frequent and fast e–n and i–n collisional channels drive all species toward a common temperature on sub-system length scales and sub-dynamical times, so we adopt a single-local-temperature closure: $T_e = T_i = T_n$.

Further, to assess spatial isothermality over the characteristic length L_0, we compare the electron conduction time $t_{\text{cond},e} \sim L^2/\chi_e$ against the dynamical time. We take χ_e to be the electron thermal diffusivity for a collisional, weakly magnetized plasma, and require $t_{\text{cond},e} \lesssim \tau_{\text{sys}}$, together with $t_{en}^{(E)} \ll \tau_{\text{sys}}$ and $t_{in}^{(E)} \ll \tau_{\text{sys}}$, to examine whether temperature perturbations are flattened faster than the flow evolves. The full set of calculated values to check these orderings is presented later in Sec. II C, and lead to the adopted conditions of thermal equilibrium among all species populations as well as spatial isothermality.

Importantly, under the spatially isothermal assumption and the ideal gas law, and in the absence of shock waves, the energy evolution equation can be omitted.

The system is modeled within a 1D axially (z) symmetric framework in cylindrical coordinates (r, θ, z), thereby considering only radial fluxes. This assumption is justified by the axisymmetric geometry of the device, where physical variations in the azimuthal (θ) direction is negligible, and as such, θ-dimension fluxes are omitted. Similarly, to assess whether any potential variation of properties in the axial (z) direction could be introduced, the Lorentz forcing components are carefully expanded and confirmed to have null forcing in the z-dimension, and no further geometric factors introduce z-dimension fluxes.

The governing model considers both radial (r) and azimuthal (θ) velocities, reflecting the plasma dynamics under ($\mathbf{E} \times \mathbf{B}$)-driven rotation in the cylindrical system. Viscosity is explicitly included in the momentum balance, ensuring that shear forces near the boundaries and dissipative losses are accounted for in the high-speed rotational system. The hydrodynamics are treated in the compressible regime, and therefore expressed in conservative form to accurately capture mass and momentum conservation laws, with dilation ($\nabla \cdot \mathbf{u}$) accounted for in the viscous stress terms. Since neutrals vastly dominate the system, the fluid viscosity is calculated from the kinetic theory of neutral gases.

The system boundary in our analysis is defined as the boundary between the plasma bulk and plasma sheath. A scale analysis of sheath magnetization based on the ratio of gyro radius to Debye length indicates $\rho_i \gg \lambda_D$ (ions unmagnetized at the sheath scale) and $\rho_e \gtrsim \lambda_D$ (at most weak electron magnetization). Accordingly, any magnetic pre-sheath is very weak and its influence on the bulk momentum balance is negligible in the present model. The MHD model pertains to the bulk plasma, whereby the quasi-neutrality assumption ($n_e \approx n_i$) applies. Electron inertia is reasonably neglected in the conservation equations. The plasma sheath width is calculated to be on the order of micrometers (taken as 1–$10\lambda_D$ as per the literature[26]) and so the spatial domain is taken to be approximately the full domain between the inner wall at R_1 and the outer wall at R_2. The width of the hydrodynamic boundary layer is assessed to be much greater than the plasma sheath

width, and therefore, no-slip velocity boundary conditions remain appropriate.

B. Governing MHD model

Based on the detailed assessment of governing assumptions, we write the 1D, axisymmetric, compressible, generalized single–fluid MHD equations in conservative form. We first present a compact vector form, in order to clearly highlight the term origins by separating (i) inviscid fluxes, and (ii) viscous stresses, both cast for a cylindrical geometry, (iii) purely geometric (curvature/metric) contributions of the cylindrical coordinates, and (iv) the decoupled electromagnetic forcing terms.

The compact vector form can be expressed as follows:

$$\frac{\partial \mathbf{U}}{\partial t} + \frac{1}{r}\frac{\partial}{\partial r}(r\,\mathbf{F}) + \frac{1}{r}\frac{\partial}{\partial r}(r\,\mathbf{F}_{\text{visc}}) = \mathbf{S}_{\text{geom}} + \mathbf{S}_{\text{MHD}}, \tag{1}$$

with

$$\mathbf{U} = \begin{bmatrix} \rho \\ \rho u_r \\ \rho u_\theta \end{bmatrix}, \quad \mathbf{F} = \begin{bmatrix} \rho u_r \\ \rho u_r^2 + p \\ \rho u_r u_\theta \end{bmatrix}, \quad \mathbf{F}_{\text{visc}} = \begin{bmatrix} 0 \\ \tau_{rr} \\ \tau_{\theta r} \end{bmatrix},$$

$$\mathbf{S}_{\text{geom}} = \begin{bmatrix} 0 \\ \dfrac{\rho u_\theta^2}{r} + \dfrac{\tau_{\theta\theta}}{r} \\ -\dfrac{\rho u_r u_\theta}{r} - \dfrac{\tau_{r\theta}}{r} \end{bmatrix}, \quad \mathbf{S}_{\text{MHD}} = \begin{bmatrix} 0 \\ (\mathbf{J}\times\mathbf{B})\cdot\hat{\mathbf{r}} \\ (\mathbf{J}\times\mathbf{B})\cdot\hat{\boldsymbol{\theta}} \end{bmatrix}.$$

Expansion of the radial fluxes on a cylindrical fluid element from the compact notation, e.g., $\frac{1}{r}\frac{\partial}{\partial r}(r\,\mathbf{F})$ produces additional terms via the product rule when differentiating. Separately, the entries of $\mathbf{S}_{\text{geom}}$ arise directly from cylindrical geometry and induced curvature effects. These consist of: in the r–momentum balance, $\rho u_\theta^2/r$ is the centrifugal term, and $\tau_{\theta\theta}/r$ is the viscous hoop–stress curvature term. In the θ–momentum balance, $-\rho u_r u_\theta/r$ is a Coriolis–like term, and $-\tau_{r\theta}/r$ is the corresponding viscous metric contribution.

For a Newtonian fluid with dynamic viscosity μ and bulk viscosity given by Stokes' hypothesis

$$\tau_{ij} = \mu\left(\partial_i u_j + \partial_j u_i - \frac{2}{3}\delta_{ij}\,\nabla\cdot\mathbf{u}\right).$$

After fully expanding and regrouping the active system terms in our coordinate system (shown in Appendix B), we arrive at the following set of equations. We keep here the RHS Lorentz forcing terms in compact notation until they can be expanded with respect to the appropriate electric current formulation defined in Sec. II C

$$\begin{aligned}
&\frac{\partial \rho}{\partial t} + \frac{\partial}{\partial r}(\rho u_r) + \frac{\rho u_r}{r} = 0,\\
&\frac{\partial(\rho u_r)}{\partial t} + \frac{\partial}{\partial r}\left(\rho u_r^2 + p\right) + \frac{p}{r} + \frac{\rho}{r}(u_r^2 - u_\theta^2)\\
&\quad + \frac{4}{3}\mu\left(\frac{\partial^2 u_r}{\partial r^2} + \frac{1}{r}\frac{\partial u_r}{\partial r} - \frac{u_r}{r^2}\right) = (\mathbf{J}\times\mathbf{B})\cdot\hat{\mathbf{r}},\\
&\frac{\partial(\rho u_\theta)}{\partial t} + \frac{\partial}{\partial r}(\rho u_r u_\theta) + \frac{2\rho u_r u_\theta}{r} + \mu\left(\frac{\partial^2 u_\theta}{\partial r^2} + \frac{1}{r}\frac{\partial u_\theta}{\partial r} - \frac{u_\theta}{r^2}\right)\\
&\quad = (\mathbf{J}\times\mathbf{B})\cdot\hat{\boldsymbol{\theta}}.
\end{aligned} \tag{2}$$

Since we determine the electric field from Ohm's law rather than evolving Maxwell's displacement current, we additionally impose current conservation as a constraint [charge continuity in the quasi-neutral limit: $\rho_c(r) = e(n_i(r) - n_e(r)) = 0$]

$$\frac{1}{r}\frac{\partial}{\partial r}(r\,J_r) = 0, \tag{3}$$

and the ideal–gas law closes the system under the isothermal LTE assumption

$$p_s = \rho_s R_s T, \quad s \in \{n, i, e\},$$

with T uniform and $p = \sum_s p_s$.

μ is taken to be the dynamic viscosity of neutral atomic hydrogen, since the neutrals are the dominant species in the plasma. The dynamic viscosity of the single fluid system can therefore be well-approximated using kinetic theory for gases, and is given by

$$\mu = \frac{5}{16}\frac{\sqrt{\pi m_i k_B T}}{\sigma_c}, \tag{4}$$

where σ_c is the collision cross section for neutral hydrogen atoms.

C. Electric field and current formulation

Here, we examine which formulation most suitably governs the electric field and current.

In the presence of an imposed magnetic field, and because high velocities, as well as large density and pressure gradients are anticipated, we adopt a formulation for the effective electric field that comprises: (i) the static potential, (ii) a motional electromotive force (EMF), and (iii) the "battery" contribution from the electron pressure gradient. (The terminology battery is adopted since this term can drive current with no applied voltage.)

The system should accurately capture an anisotropic electrical response in the magnetized, partially ionized plasma, and we therefore adopt a tensorial conductivity. With ion–neutral co-motion, the electric current in a quasi-neutral plasma is closed by the following generalized single-fluid Ohm's law:

$$\mathbf{J} = \tilde{\sigma}\cdot\left(-\nabla\phi + \mathbf{u}\times\mathbf{B} - \frac{1}{en_e}\nabla p_e\right), \tag{5}$$

where

$$\tilde{\sigma} = \begin{bmatrix} \sigma_P & -\sigma_H & 0 \\ \sigma_H & \sigma_P & 0 \\ 0 & 0 & \sigma_\parallel \end{bmatrix}. \tag{6}$$

$\tilde{\sigma}$ is the conductivity tensor, where its components: σ_P is the Pedersen conductivity, representing the component of conductivity in the plane perpendicular to the magnetic field, aligned with the electric field. σ_H is the Hall conductivity, representing the component of conductivity perpendicular to both the electric and magnetic fields, leading to a Hall current. $\sigma_\parallel$ is the parallel conductivity along the magnetic field (along the z axis in this case).

Where the active system components are $\mathbf{B} = (0, 0, B_z)$ and $\mathbf{E} = (E_r, 0, 0)$, the component expansion of active terms in the Lorentz forcing terms $(\mathbf{J}\times\mathbf{B})\cdot\hat{\mathbf{r}}$ and $(\mathbf{J}\times\mathbf{B})\cdot\hat{\boldsymbol{\theta}}$ are given by

$$(\mathbf{J}\times\mathbf{B})\cdot\hat{\mathbf{r}} = J_\theta B_z = \sigma_H\cdot\left[-\frac{\partial\phi}{\partial r}+u_\theta B_z+\frac{1}{n_e e}\frac{\partial p_e}{\partial r}\right]\cdot B_z-\sigma_P u_r B_z^2,$$
$$(\mathbf{J}\times\mathbf{B})\cdot\hat{\boldsymbol{\theta}} = -J_r B_z = -\sigma_P\cdot\left[-\frac{\partial\phi}{\partial r}+u_\theta B_z+\frac{1}{n_e e}\frac{\partial p_e}{\partial r}\right]\cdot B_z+\sigma_H u_r B_z^2. \quad (7)$$

We find for the active electric and magnetic field components that $(\mathbf{J}\times\mathbf{B})\cdot\hat{\mathbf{z}}=0$ which confirms no additional Lorentz-force-induced z-momentum components, and the system remains purely 1D-axisymmetric.

Accordingly, the charge continuity equation presented in (3) becomes

$$\frac{1}{r}\frac{\partial}{\partial r}\left[r\sigma_P\left(-\frac{\partial\phi}{\partial r}+u_\theta B_z+\frac{1}{n_e e}\frac{\partial p_e}{\partial r}\right)+r\sigma_H u_r B_z\right]=0. \quad (8)$$

D. Electrical conductivity formulation

In a weakly ionized plasma, the presence of a magnetic field induces anisotropy in the electrical conductivity by altering the motion of charged particles. Charged particles undergo gyro-motion around magnetic field lines, and their drift propagation is influenced by collisions, which disrupt this motion and scatter the particles. The interplay between gyro-frequencies and collision frequencies determines the degree of anisotropy in the plasma, shaping the Hall and Pedersen conductivities.

In the case of multiple species, the Hall and Pedersen conductivities should be treated as the sum of contributions from each species s_1 interacting with another species s_2, where we consider the contributions of all ion, neutral, and electron species

$$\sigma_P=\sum_{s_1,s_2}\frac{q_{s_1}^2 n_{s_1}}{m_{s_1}}\frac{\nu_{s_1s_2}}{\nu_{s_1s_2}^2+\omega_{cs_1}^2},\quad \sigma_H=\sum_{s_1,s_2}\frac{q_{s_1}^2 n_{s_1}}{m_{s_1}}\frac{\omega_{cs_1}}{\nu_{s_1s_2}^2+\omega_{cs_1}^2}, \quad (9)$$

where q_s is the signed value of the species charge (i.e., $q=Ze$, where Z is the $\pm$ ionization state, naturally $Z=0$ for neutral species), n_s is the species number density, and m_s is the species mass.

$\nu_{s_1s_2}$ is the collision frequency between species, which is directional and proportional to the secondary species density (n_{s_2}) and the relevant cross section ($\sigma_{s_1s_2}$)

$$\nu_{s_1s_2}=n_{s_2}\langle\sigma_{s_1s_2}v\rangle, \quad (10)$$

where $\langle\sigma_{s_1s_2}v\rangle$ is the average species-species collision rate coefficient. v is the relative velocity between particles: however, this must consider both the thermalized motion of the particles which is assumed to be Maxwellian for both species as well as the bulk relative motion of the species. Since we have established that the relative bulk motion is zero in our system, v is simply $v_{thermal}$

$$v_{\text{thermal}}=\sqrt{\frac{8k_BT}{\pi m_r}}. \quad (11)$$

The ion cyclotron frequency is the angular frequency of ion gyration in a magnetic field and given by

$$\omega_{cs_1}=\frac{qB}{m_{s_1}}, \quad (12)$$

where B is the magnetic field strength.

While ion–neutral collisions (ν_{in}) typically dominate momentum exchange due to the abundance of neutral particles, electron–neutral collisions also play a significant role because of the high mobility of electrons ($m_e\ll m_i$), which significantly contributes to the total current. In this analysis, we therefore consider all relevant contributions for collisions: ion–neutral, electron–neutral, and ion–electron.

The relevant Pedersen conductivity is given by

$$\sigma_P=\frac{n_iq_i^2\nu_{in}}{m_i(\nu_{in}^2+\omega_{ci}^2)}+\frac{n_eq_e^2\nu_{en}}{m_e(\nu_{en}^2+\omega_{ce}^2)}+\frac{n_iq_i^2\nu_{ie}}{m_i(\nu_{ie}^2+\omega_{ci}^2)}+\frac{n_eq_e^2\nu_{ei}}{m_e(\nu_{ei}^2+\omega_{ce}^2)}. \quad (13)$$

The ion–electron interaction terms in the Hall conductivity formulation, however, are of equal magnitude and opposite sign (since the cyclotron frequency is directionally determined by the particle charge Z), and therefore directly cancel one another. The relevant Hall conductivity is therefore given by

$$\sigma_H=\frac{n_iq_i^2\omega_{ci}}{m_i(\nu_{in}^2+\omega_{ci}^2)}+\frac{n_eq_e^2\omega_{ce}}{m_e(\nu_{en}^2+\omega_{ce}^2)}, \quad (14)$$

where the ion cyclotron frequency is the angular frequency of ion gyration in a magnetic field given by $\omega_{cs}=\frac{q_sB}{m_i}$, and since we assume quasi-neutrality ($n_e\approx n_i$) and because the ion species are singly ionized $|q_e|=q_i=e$, then we arrive at the expression

$$\sigma_H=e^3B\left[\frac{n_i}{m_i(\nu_{in}^2+\omega_{ci}^2)}-\frac{n_e}{m_e(\nu_{en}^2+\omega_{ce}^2)}\right]. \quad (15)$$

For collisions with neutrals, the cross sections σ_{in}, σ_{en} are (reasonably) known constants with assumed values taken from the literature[27] and reported in Table I. For electron–ion collisions, however, it is a little more complicated. Ion–electron collisions are governed by

TABLE I. Values of constants and fixed parameters.

Symbol	Definition	Value
e	Charge of a proton	1.602×10^{-19} C
m_i	Mass of a proton	1.67×10^{-27} kg
m_e	Mass of an electron	9.11×10^{-31} kg
k_B	Boltzmann constant	1.38×10^{-23} J/K
h	Planck's constant	6.36×10^{-34} Js
σ_c	Collision cross section for neutral hydrogen atoms ($T=0.5$ eV)	1.05×10^{-18} m^2
σ_{in}	Ion–neutral elastic collision cross section ($T=0.5$ eV)	1.96×10^{-18} m^2
σ_{en}	Electron–neutral elastic collision cross section ($T=0.5$ eV)	1.16×10^{-19} m^2
R_s	Specific gas constant for atomic hydrogen	4124.24 J/kg/K
ε	Ionization energy of hydrogen	13.6 eV
(g_0,g_1)	Degeneracy factors for a neutral and singly ionized atom	(1, 1)

Coulomb interactions, leading to a velocity-dependent cross section. The effective cross section can be expressed as

$$\nu_{ie} = n_e \langle \sigma_{ie} v \rangle, \tag{16}$$

where

$$\sigma_{ie} \propto \frac{e^4}{\varepsilon_0^2 m_e^2 v^4}. \tag{17}$$

The collision frequency for Coulomb collisions is given by the formalism[28]

$$\nu_{ie} \approx \frac{n_e e^4 \cdot 4\pi \ln \Lambda}{\varepsilon_0^2 m_e^2 v^3}, \tag{18}$$

where $(\ln \Lambda)$ is the Coulomb logarithm which can be calculated from

$$\ln \Lambda = \ln \left(\frac{\lambda_D}{b_{90}} \right), \tag{19}$$

where λ_D is the plasma Debye length and b_{90} is the classical 90° deflection impact parameter

$$\lambda_D = \sqrt{\frac{\varepsilon_0 k_B T_e}{n_e e^2}}, \quad b_{90} = \frac{e^2}{4\pi\varepsilon_0 m_r v_{th}^2}. \tag{20}$$

E. Dissociation and ionization models

We ensure the system is thermodynamically consistent, whereby the degree of neutral dissociation and further plasma ionization is calculated for the system's initial pressure and temperature. The Saha equation[29] describes the ratio of different ionization states in a gas under thermodynamic equilibrium. However, it can also be adapted to describe molecular dissociation processes, such as the dissociation of molecular hydrogen (which is an equilibrium process in our system). The dissociation form is given by

$$\frac{n_H}{n_{H_2}} = \frac{Q_H}{Q_{H_2}} \frac{2}{P} \left(\frac{2\pi m_H k_B T}{h^2} \right)^{3/2} \exp\left(-\frac{D}{k_B T} \right). \tag{21}$$

In this expression, n_H and n_{H_2} denote the number densities of atomic and molecular hydrogen, respectively. The quantities Q_H and Q_{H_2} represent the partition functions of atomic and molecular hydrogen (please refer to Appendix A for details). P is the total pressure of the system, m_H is the mass of a hydrogen atom, k_B is Boltzmann's constant, h is Planck's constant, and T is the assumed neutral temperature. The parameter $D = 4.48$ eV corresponds to the dissociation energy of molecular hydrogen, i.e., the energy required to break an H_2 molecule into two hydrogen atoms.

It is found that the ratio n_H/n_{H_2} exceeded 10^8. We, therefore, conclude that, under the fill pressure and at the assumed heavy-particle plasma temperature, the neutral component of the plasma consists overwhelmingly of atomic hydrogen.

The Saha equation is again applied (in its standard form) to calculate the degree of ionization in a gas in thermal equilibrium. It is particularly applicable for determining the ionization degree of weakly ionized plasmas, where the Debye length is small, ensuring minimal Coulomb screening.

When only the first level of ionization is significant, as per the case for a weakly ionized atomic hydrogen plasma, the Saha equation simplifies to

$$\frac{n_e^2}{n - n_e} = \frac{2}{\lambda_{th}^3} \frac{g_1}{g_0} \exp\left(-\frac{\varepsilon}{k_B T} \right), \tag{22}$$

where n is the total atomic density (sum of neutral and ionized particles, $n = n_n + n_e$), n_e is the electron density, equivalent to n_1 (density of singly ionized atoms) since each ion contributes one free electron, and therefore $n_e = n_i$ as per the quasi-neutrality assumption. g_0, g_1 are degeneracy factors for neutral and singly ionized atoms, respectively, ε is the ionization energy of the atom.

λ_{th} is the thermal de Broglie wavelength of an electron, given by

$$\lambda_{th} = \frac{h}{\sqrt{2\pi m_e k_B T}}, \tag{23}$$

where h is the Planck's constant, and m_e is the electron mass.

The degree of ionization, x, is defined as the fraction of atoms that are ionized, which can be written as follows:

$$x = \frac{n_i}{n_n + n_i} = \frac{n_i}{n} = \frac{n_e}{n}. \tag{24}$$

Rewriting the Saha equation then in terms of x

$$\frac{x^2}{1 - x} = A, \tag{25}$$

where

$$A = \frac{2}{n\lambda_{th}^3} \frac{g_1}{g_0} \exp\left(-\frac{\varepsilon}{k_B T} \right) \tag{26}$$

gives the quadratic equation: $x^2 + Ax - A = 0$, which can simply be solved under varying n values with all variables otherwise constant.

F. Steady-state plasma model

We now impose a steady state on the expanded system in (2). In the physical system, the Lorentz forcing accelerates the plasma until the azimuthal momentum asymptotes to a constant profile. This finalized steady state is in a hydrostatic pressure-balanced equilibrium, which implies the radial velocity has equilibrated to zero.

Physically, the Lorentz force drives azimuthal motion that relaxes to a time-independent profile in which Lorentz forcing is balanced by viscous diffusion of angular momentum. In the radial direction, the solution approaches a static force balance while the radial mass flux decays to zero; with impermeable boundaries this yields $u_r(r) = 0$ across the annular space.

Accordingly, the steady-state conditions are:

(1) Time independence

$$\frac{\partial \rho}{\partial t} = 0, \quad \frac{\partial (\rho u_r)}{\partial t} = 0, \quad \frac{\partial (\rho u_\theta)}{\partial t} = 0.$$

(2) No radial through–flow

$$u_r(r) \equiv 0.$$

Applying these conditions, the mass continuity equation approaches zero in the steady state. The expanded ion-radial-momentum

equation reduces to a static force balance between hydrostatic pressure, centrifugal forcing, and a radial Lorentz forcing component. Meanwhile, the azimuthal momentum equation balances viscous diffusion against Lorentz force-driven angular momentum in the steady state. Finally, the charge continuity equation expanded in Eq. (8) can also be reduced.

The resultant steady-state equations are given as such

$$\begin{aligned}
&\frac{\partial p}{\partial r} - \frac{\rho u_\theta^2}{r} + \frac{p}{r} = \sigma_H \cdot \left[-\frac{\partial \phi}{\partial r} + u_\theta B_z + \frac{1}{n_e e}\frac{\partial p_e}{\partial r} \right] \cdot B_z, \\
&\mu\left(\frac{\partial^2 u_\theta}{\partial r^2} + \frac{1}{r}\frac{\partial u_\theta}{\partial r} - \frac{u_\theta}{r^2} \right) = -\sigma_P \cdot \left[-\frac{\partial \phi}{\partial r} + u_\theta B_z + \frac{1}{n_e e}\frac{\partial p_e}{\partial r} \right] \cdot B_z, \\
&\frac{\partial}{\partial r}\left(r\sigma_P \frac{\partial \phi}{\partial r} \right) = B_z \frac{\partial}{\partial r}(r\sigma_P u_\theta) + \frac{\partial}{\partial r}\left(\frac{r\sigma_P}{n_e e}\frac{\partial p_e}{\partial r} \right).
\end{aligned} \tag{27}$$

The system is thermodynamically closed via: $p_s = x_s \rho R_s T$, where x_s is the species ionization fraction.

Importantly, we impose one more known condition on the system for the solution. From the known total experimental current I_0, we impose the condition of constant total electric current by invoking current conservation across coaxial cylindrical shells. Under the assumptions of radial symmetry, steady-state operation, and the absence of internal current sources or sinks, the same total current I_0 must flow through every cylindrical surface between the inner radius R_1 and outer radius R_2, whereby

$$J_r(r) = \sigma_P \left(-\frac{\partial \phi}{\partial r} + B_z u_\theta + \frac{1}{n_e e}\frac{\partial p_e}{\partial r} \right) = \frac{I_0}{2\pi r L}. \tag{28}$$

Here, I_0 is the total current set as a steady input in the experiments, and L is the axial length of the cylindrical device.

We discuss and apply boundary conditions during the solution steps.

III. SEMI-ANALYTICAL SOLUTION

A. Solution of the steady-state model

Here, we present the analytical solution of the steady-state model defined by the coupled system Eqs. (27) and (28), in terms of the unknown radial profiles of the critical plasma properties: $\phi(r), u_\theta(r), \rho(r), p(r)$

Starting with the treatment of $\frac{\partial \phi}{\partial r}$ in the final equation of (27), and by collecting all terms where the total radial derivative applies, the RHS vanishes, and therefore the enclosed quantity of the total derivative is a constant. We therefore arrive at the following equation form where the constant C_0 is made explicit:

$$\frac{\partial \phi}{\partial r} = B_z u_\theta + \frac{1}{n_e e}\frac{\partial p_e}{\partial r} - \frac{C_0}{r\sigma_P}, \tag{29}$$

the constant C_0 can be directly solved for by equating Eq. (29) with the imposed fixed current Eq. (28)

$$C_0 = \frac{I_0}{2\pi L}. \tag{30}$$

Further integration steps cannot be conducted without a known expression for $u_\theta(r)$, and so from here we proceed by solving for azimuthal velocity. We can similarly substitute the known $J_r(r)$ expression into the azimuthal momentum equation and simplify for analysis via a variable substitution for grouped constants

$$\frac{\partial^2 u_\theta}{\partial r^2} + \frac{1}{r}\frac{\partial u_\theta}{\partial r} - \frac{u_\theta}{r^2} = -\frac{\beta}{r}, \tag{31}$$

where

$$\beta = \frac{I_0 B_z}{\mu \cdot 2\pi L}. \tag{32}$$

Note that the term β physically represents the ratio of applied Lorentz forcing (current × applied **B**-field) in the system, to resistive viscous force dissipation in the system (viscosity × effective area term).

Equation (31) is a second-order linear inhomogeneous differential equation. where the homogeneous part is a Cauchy–Euler equation and can be solved via a power law substitution, where we arrive at

$$u_{\theta,\text{homogeneous}}(r) = D_1 r + \frac{D_2}{r}. \tag{33}$$

The particular solution is obtained by substituting the equation form $u_{test} = Ar\ln(r)$, and arriving at

$$u_{\theta,\text{particular}}(r) = \frac{-\beta}{2} r \ln(r), \tag{34}$$

which therefore gives the total solution

$$u_\theta(r) = D_1 r + \frac{D_2}{r} - \frac{1}{2}\beta r \ln(r), \tag{35}$$

where D_1 and D_2 are constants which can be solved by applying boundary conditions on $u_\theta(r)$.

Our problem exists in the domain $r \in [R_1, R_2]$, and since we have modeled a viscous system, we must apply the no-slip condition at the boundaries for physical consistency

$$u_\theta(R_1) = u_\theta(R_2) = 0.$$

The simultaneous solution of the boundary condition equations for D_1 and D_2 is non-trivial, and the analytical steps are shown in Appendix C. The final expressions are given by

$$\begin{aligned}
D_1 &= \frac{\beta\left[R_2^2 \ln(R_2) - R_1^2 \ln(R_1)\right]}{2\left(R_1^2 - R_2^2\right)}, \\
D_2 &= \frac{\beta R_2^2 R_1^2 \ln\left(\frac{R_2}{R_1}\right)}{2\left(R_1^2 - R_2^2\right)}.
\end{aligned} \tag{36}$$

Next, we advance to a solution for $\rho(r)$ from equation (*iii*) by incorporating the solution of $u_\theta(r)$. Equation (*iii*) can be re-written as

$$\frac{\partial \rho}{\partial r} = \frac{\rho u_\theta^2}{R_s T r} + \frac{\rho}{r} + \frac{\sigma_H}{\sigma_P R_s T} \cdot \frac{B_z I_0}{2\pi r L}. \tag{37}$$

We begin the analysis by observing that the governing equation for the radial derivative of the density $\rho(r)$ takes the form of a first-order, linear, non-homogeneous differential equation

$$\frac{\partial \rho}{\partial r} = A(r)\rho(r) + B(r), \tag{38}$$

where the coefficient functions $A(r)$ and $B(r)$ are defined as follows:

$$A(r) = \left(\frac{u_\theta^2}{R_s T} + 1\right) \cdot \frac{1}{r}, \quad B(r) = \frac{\sigma_H}{\sigma_P} \cdot \frac{B_z I_0}{2\pi L R_s T} \cdot \frac{1}{r}. \tag{39}$$

It is instructive to examine the ratio $B(r)/A(r)$, which represents the relative significance of the non-homogeneous term compared to the homogeneous growth rate

$$\frac{B(r)}{A(r)} = \frac{\sigma_H}{\sigma_P} \cdot \frac{B_z I_0}{2\pi L} \cdot \frac{1}{u_\theta^2 + R_s T}. \tag{40}$$

The approach taken in this section is to first solve the complete Eq. (38) *numerically*, whereby all spatially varying parameters are fully computed as such, the resultant $\rho(r)$ profile is examined with and without the additional Hall term $B(r)$.

We find that the resultant $\rho(r)$ profile is indistinguishable with and without the $B(r)$ term. Based on the numerical system solution, we compute directly the radial profile of the $\left|\frac{B(r)}{A(r)}\right|$ term as given in Eq. (40) and plot the result to examine the form and bounds. We find that across the radial space: $2.07 \times 10^{-7} < \left|\frac{B(r)}{A(r)}\right| < 4.35 \times 10^{-5}$ which is consistent with the observed indistinguishable plots for numerically computed $\rho(r)$ with and without the $B(r)$ Hall term. We conclude that $B(r)$ is physically negligible in the system, and we proceed by developing a fully analytical solution for the reduced system.

Neglecting $B(r)$, the equation reduces to a homogeneous form

$$\frac{\partial \rho}{\partial r} = A(r)\rho(r), \tag{41}$$

where this equation can be integrated directly

$$\rho(r) = \rho_0 e^{\int A(r) dr}, \tag{42}$$

and where $\rho_0 = e^{C_1}$ is a consolidated integration constant determined by boundary conditions.

In this system, the solution for $\int A(r)\, dr$ is long and complex

$$\int A(r)\, dr = \int \left[\frac{1}{r R_s T} \cdot (D_1 r + \frac{D_2}{r} - \frac{1}{2}\beta r \ln(r))^2 + \frac{1}{r}\right] dr, \tag{43}$$

and therefore shown in Appendix D. After many algebraic steps, the analytical solution is given by

$$\rho(r) = \rho_0 \cdot r^{\left(\frac{2D_1 D_2}{R_s T} + 1\right)} \cdot e^{\frac{1}{R_s T}\left[\left(\frac{1}{2}\beta D_1 r^2 - \frac{1}{8}\beta^2 r^2\right)\ln(r) + \left(\frac{1}{2}\beta D_2 + \frac{1}{8}\beta^2 r^2\right)\ln^2(r) + \left(-\frac{D_2^2}{2r^2} - \frac{1}{4}\beta D_1 r^2 + \frac{1}{16}\beta^2 r^2\right)\right]}. \tag{44}$$

Here, the constant ρ_0 represents a grouping of integration constants. The constant is solved under the important physical condition that the *total particles in the system are conserved*. From the initial fill pressure, the baseline uniform particle number density can be determined, and we establish the following relation and solve for ρ_0:

$$2\pi L \cdot \int_{R_1}^{R_2} \rho_0 r\, dr = 2\pi L \cdot \int_{R_1}^{R_2} \rho(r) r\, dr. \tag{45}$$

The RHS integral is computed numerically in the implementation simply to expedite the process of solving for ρ_0.

We can now solve the final coupled equation in (27) and determine the profile for the electric potential $\phi(r)$ in the plasma. We return to the previous partial integration resulting in Eq. (29).

Recognizing that $n_e(r) = n_i(r) = \frac{\chi_i(r)\rho(r)}{m_i}$, and for electron pressure: $p_e(r) = \chi_i(r)\rho(r)R_s T$, where the ionization fraction χ_i is a non-trivial and spatially varying function of particle density (and constant temperature) and is computed via the Saha ionization equation. χ_i is non-constant, but known, due to the solved density equation $\rho(r)$ given by (44). We can reformulate the battery electric field term as such

$$\frac{1}{n_e e}\frac{\partial p_e}{\partial r} = \frac{m_i}{\chi_i \rho e}\frac{\partial(\rho \chi_i R_s T)}{\partial r} = \frac{m_i R_s T}{e}\left(\frac{1}{\rho}\frac{\partial \rho}{\partial r} + \frac{1}{\chi_i}\frac{\partial \chi_i}{\partial r}\right), \tag{46}$$

then, taking

$$\frac{\partial \rho}{\partial r} = \left(\frac{u_\theta^2}{R_s T} + 1\right) \cdot \frac{\rho}{r}, \tag{47}$$

and noting the integral identity: $\frac{1}{\chi_i}\frac{\partial \chi_i}{\partial r} = \frac{\partial}{\partial r}\ln(\chi_i)$, then

$$\frac{m_i R_s T}{e}\left(\frac{1}{\rho}\frac{\partial \rho}{\partial r} + \frac{1}{\chi_i}\frac{\partial \chi_i}{\partial r}\right) = \frac{m_i}{e}\left(\frac{u_\theta^2 + R_s T}{r} + R_s T \frac{\partial}{\partial r}\ln(\chi_i)\right). \tag{48}$$

The equation for the static electric field in our system then becomes

$$\frac{\partial \phi}{\partial r} = B_z u_\theta + \frac{m_i}{e}\left(\frac{u_\theta^2 + R_s T}{r} + R_s T \frac{\partial}{\partial r}\ln(\chi_i)\right) - \frac{C_0}{r\sigma_P}, \tag{49}$$

where $C_0 = \frac{I_0}{2\pi L}$ is a constant, while χ_i and σ_P are both complex functions of other known variables. The solution for $\phi(r)$ is given by the integral

$$\phi(r) = \int \left[B_z u_\theta + \frac{m_i}{e}\left(\frac{u_\theta^2 + R_s T}{r} + R_s T \frac{\partial}{\partial r}\ln(\chi_i)\right) - \frac{C_0}{r\sigma_P}\right] dr, \tag{50}$$

where a boundary condition is applied such that the outer cathode wall is grounded, consistent with the experimental condition

$$\phi(R_2) = 0. \tag{51}$$

Unlike the earlier MHD variables $u_\theta(r)$ and $\rho(r)$ which can be expressed directly as a function of constant terms and r, the solution of $\phi(r)$ requires the intermediate solution of terms $\chi_i(r)$ and $\sigma_P(r)$—which are themselves functions of the local plasma state—and cannot be integrated analytically for solution in Eq. (E1). Therefore, we proceed with the staged numerical solution of $\phi(r)$ described as follows:

(1) **Radial discretization:** Discretise $[R_1, R_2]$ on a 1D monotone grid $\{r_j\}_{j=0}^{N}$. N is sufficiently large that the solution has reasonably converged.
(2) **Direct analytic solutions:** Evaluate discrete $u_\theta(r_j)$ and $\rho(r_j)$ directly from the derived analytical formulas.
(3) **Local solutions for ionization and conductivity:** At each r_j, compute the ionization fraction $\chi_i(r_j)$ from the Saha relation at the single temperature T. Further, compute $\sigma_P(r_j)$ using the Pederson conductivity model with local $\rho(r_j), n_e(r_j)$, and B_z (const). The Coulomb logarithm can be evaluated from the local Debye length.

(4) **Finite difference derivative term:** The derivative $\partial_r \ln \chi_i$ is computed via a second-order central finite difference method applied to $\ln(\max[\chi_i, x_{\min}])$

$$\left.\frac{\partial}{\partial r}\ln \chi_i\right|_{r_j} \approx \frac{\ln \chi_i(r_{j+1}) - \ln \chi_i(r_{j-1})}{r_{j+1} - r_{j-1}},$$

with one-sided formulas at the boundaries.

(5) **Integrand term:** The RHS integrand defined on the discrete grid is given by

$$f(r_j) = B_z\, u_\theta(r_j) + \frac{m_i}{e}\left[\frac{u_\theta(r_j)^2 + R_s T}{r_j} + R_s T \left.\frac{\partial}{\partial r}\ln \chi_i\right|_{r_j}\right] - \frac{C_0}{r_j\, \sigma_P(r_j)}. \tag{52}$$

(6) **Numerical integration:** The solution for $\phi(r)$ is then purely integrative, and is computed via the cumulative integral applying the composite trapezoidal rule

$$I(r_j) = \int_{R_1}^{r_j} f(s)\, ds \approx \sum_{k=1}^{j} \frac{1}{2}(f_{k-1} + f_k)\,(r_k - r_{k-1}).$$

(7) **Boundary condition:** Enforce the grounded outer wall constraint $[\phi(R_2) = 0]$ by a constant shift

$$\phi(r_j) = I(r_j) - I(R_2),$$

which is algebraically identical to $\phi(r) = \int_{R_2}^{r} f(s)\, ds$.

B. Fixed parameters, input variables, and computed variables

The values of known constants and fixed parameters used throughout the analysis are listed in Table I. There is some variation in collisional cross sections use in the literature for neutral, ion, and electron collisions. For the electron–hydrogen collisional cross section (σ_{en}), we adopt the precise value from the detailed review by Yoon *et al.*,[30] and for the ion–neutral collisional cross section (σ_{in}) and neutral hydrogen cross section (σ_c) we adopt the values reported by Vranjes and Krstic[31] at $T = 0.5$ eV.

We define here a set of default inputs into the system. We later study the effects of varying such parameters; however, they otherwise are assumed to take on the default values represented in Table II.

From these physically based input conditions, all other parameters are calculated fully self-consistently as per the presented model.

TABLE II. Experimental input parameters—default values.

Symbol	Definition	Value
P_{fill}	Chamber fill pressure	3 Torr
n_n	Initial uniform plasma neutral density	1.0×10^{22} m^{-3}
T	Isothermal plasma temperature	0.5 eV
I_0	Total radial plasma current	20 A
B_z	Axial magnetic field strength	0.35 T
R_1	Inner radial distance of cylindrical anode	0.0472 m
R_2	Outer radial distance of cylindrical cathode	0.0725 m
L_0	Axial length of plasma disk ($\hat{z}$)	0.0127 m

C. Default conditions: System solution and discussion

We present the full solution for the steady-state, one-dimensional MHD system, under the default conditions—matched with the default experimental run condition. We first show the radial profiles of the principal MHD variables: azimuthal velocity $u_\theta(r)$, $\rho(r)$ is converted directly to species particle densities $n_s(r) = \frac{x_s(r)\rho(r)}{m_s}$, and electric potential $\phi(r)$. We then present additional variables which develop a radial profile, and are of interest for examining the underlying plasma state of the system: ionization fraction $\chi_i(r)$ and Pederson and Hall conductivities $\sigma_P(r), \sigma_H(r)$. Further, we can break down the electric fields and currents by contributing components.

To support the physical interpretation and provide intuitive spatial insight into the plasma, we begin with a rendered 3D visualization of the default solution. Although the system solution is fundamentally one-dimensional in the radial direction, it represents a 3D axisymmetric system. Therefore, the visualization is constructed by revolving the radial solution about the axial (z-) axis, and extruding along the z-direction to provide a full volumetric perspective, depicting the θ and z-invariant solution. We present in parallel in Fig. 4 the direct 1D profiles.

Figure 4(a) depicts the azimuthal velocity, and by comparison to the acoustic velocity, we observe that the plasma is supersonic over most of the central region of the annular space. The shape of the velocity profile is not dissimilar from studies of related systems such as the ring-offset-anode plasma centrifuge.[2] We observe a subtle right skew in the arcing profile, with peak velocity situated closer to the inner anode at approximately $r = 0.0598$ m—consistent with the relatively larger volume of fluid at the outer radial points under cylindrical geometry. Over the time for a steady state to form, a far reaching shear profile is established to form an equilibrium which balances the driving Lorentz force with viscous dissipation. This can be understood through the inhomogeneous β RHS driving term in the derived analytical equation, which operates on the LHS function of u_θ to establish a steady-state velocity profile

$$\beta = \frac{\text{Lorentz forcing}}{\text{Viscous dissipation}} = \frac{I_0 B_z}{\mu \cdot 2\pi L}. \tag{53}$$

Consistent with the finding that the plasma velocity profile is supersonic, Fig. 4(b) shows substantial radial compression of the bulk plasma. The profile exhibits a steep, sigmoidal rise in density toward the outer radius, characteristic of strong centrifugal compression. Recalling the governing constraint that the total number of particles in the system is conserved, this outer compression is necessarily balanced by a corresponding rarefaction in the inner region (the integral of the density profile remains equal between initial and final states). Inspecting the terms present in the governing equation, and considering the analysis that found the transverse (Hall) Lorentz forcing term to be negligible, we understand that the radial profile exhibits the dynamic equilibrium between dominant centrifugal forcing and hydrostatic pressure, resulting in mass redistribution without net particle gain or loss.

Figure 5 further investigates the specific particle densities (neutrals and ions), which are interdependent with the degree of ionization in the system (itself a function of system pressures). Due to the relatively higher ionization degree at the rarefied inner radial region, we find the *ion* species density exhibits a marginally weaker gradient

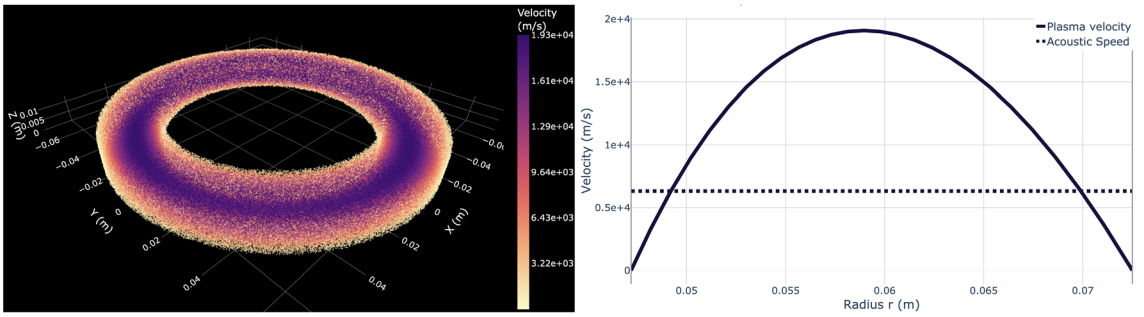

(a) Azimuthal plasma velocity $u_\theta(r)$ solution.

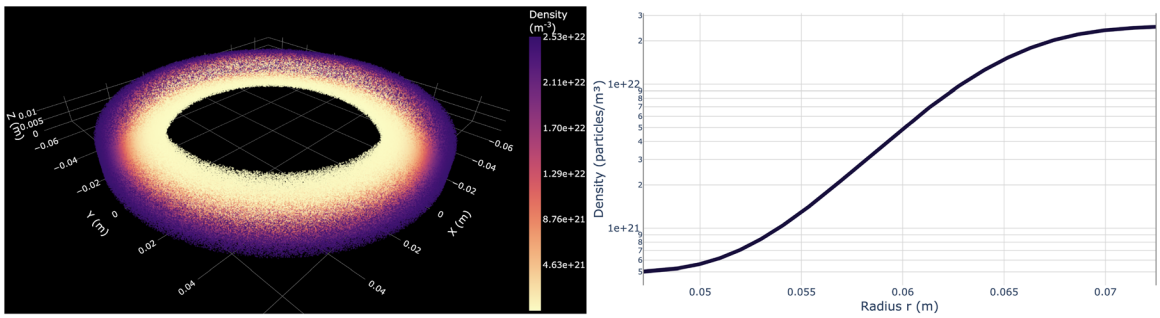

(b) Total particle density $n_{total}(r)$ solution.

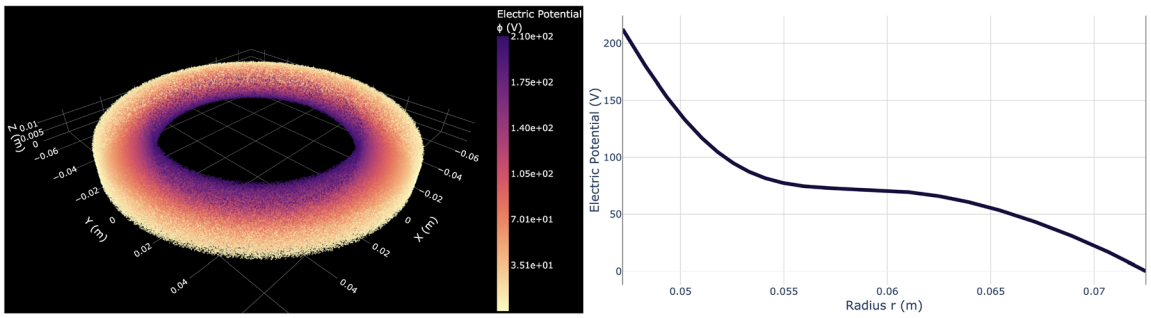

(c) Plasma electric potential $\phi(r)$ solution

FIG. 4. 3D plots: the computed values of each plasma variable are illustrated using a colored heat map, where sample points from the radial profile are distributed across the rendered true geometry. The heat map represents the property value in space. 1D plots show the direct 1D line solution from which the 3D equivalent system is constructed.

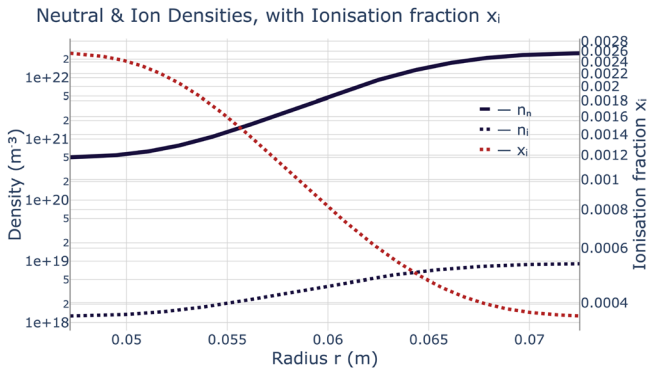

FIG. 5. Comparison of neutral particle density to ion particle density, as a function of ionization fraction $\chi_i(r)$ shown on the dual axis.

overall (and resulting outer–inner particle ratio) as compared to the neutral species.

We define two complementary measures of compression ratio. The first is the total contrast ratio, given by the ratio of maximum to minimum particle density across the domain. The second is the baseline-relative compression ratio, which measures the peak density rise above the uniform baseline reference state, where the reference state is calculated from the initial fill pressure density. Together, these metrics provide a clear quantitative description of the compression induced by the plasma's rotational dynamics. Both definitions are reported in Table III, and as per the profiles observed in Fig. 5, we see more modest compression ratios (both contrast and baseline-relative) for the ion-species.

The computed electric potential profile reveals a clear and continuous voltage drop across the bulk plasma. This behavior is characteristic of a resistive plasma, in contrast to the idealized case of a perfect

TABLE III. Key output quantities from steady-state solution.

Quantity	Symbol	Value
Peak velocity	V_{peak}	$1.91 \times 10^{4}\ \text{ms}^{-1}$
Peak rotational velocity	ω_{peak}	$3.19 \times 10^{5}\ \text{rads}^{-1}$
Radius at peak velocity	R_{peak}	$5.99 \times 10^{-2}\ \text{m}$
Period of peak rotation (at R_{peak})	τ_{sys}	$1.97 \times 10^{-5}\ \text{s}$
Peak density	n_{peak}	$2.50 \times 10^{22}\ \text{m}^{-3}$
Total voltage drop	$\Delta\phi$	$2.13 \times 10^{2}\ \text{V}$
Peak centrifugal acceleration	a_{peak}	$6.21 \times 10^{9}\ \text{ms}^{-2}$
Bulk throughput power	$\text{Power}_{\text{total}}$	$4.25 \times 10^{3}\ \text{W}$
Neutral compression ratio	$n_{n,\max}/n_{n,\min}$	5.00×10^{1}
Neutral compression ratio	$n_{n,\max}/n_{n,\text{baseline}}$	2.50×10
Ion compression ratio	$n_{i,\max}/n_{i,\min}$	7.08×10
Ion compression ratio	$n_{i,\max}/n_{i,\text{baseline}}$	1.58×10

conductor in which the electric field would vanish within the bulk. In weakly ionized plasmas, such as the one studied here, this finite field arises due to collisional momentum transfer between electrons and the background neutral gas. As electrons move rapidly due to applied fields and their thermal energy, their frequent scattering with neutrals introduces effective resistivity, thereby sustaining a non-zero electric field through the bulk even in steady state.

We can further examine the components of the electric field and current in Figs. 6 and 7. Recalling that

$$J_{r,\text{total}} = \sigma_p(E_{\text{static}} + E_{\text{motional}} + E_{\text{battery}}), \tag{54}$$

and observing that the computed solution of σ_P in Fig. 6 is, interestingly, non-monotonic, one can understand the contributions toward the total effective current which obeys the charge continuity law in cylindrical geometry. Note that in the direct plot of the static potential field $\phi(r)$ in Fig. 4(c), we see initially a steeper potential drop near the inner anode, a central region of relative plateau—corresponding to elevated electrical conductivity and smaller static electric field—before a negative gradient is established again closer to the outer cathode. By comparing this profile to $J_{\text{static}} = -\sigma_P \cdot \frac{\partial\phi}{\partial r}$ one can observe by inspection that the plateau in ϕ corresponds with the point of minimum static electric potential field in the plasma. The electric current

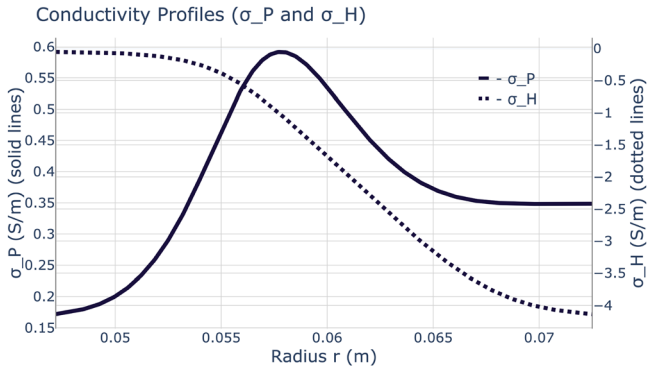

FIG. 6. Profiles for Pederson and Hall conductivities across the radial space.

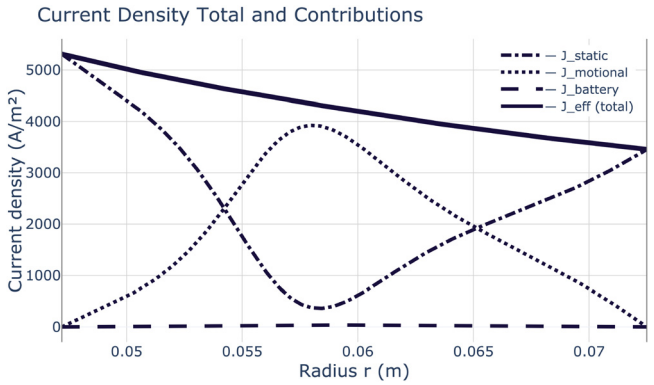

FIG. 7. Total effective electric current and component contributions across the radial space.

continuity in the central region is supported primarily by the motional electric field (driven by $u_\theta B_z$), where velocity is near its maximum. One should also note that the E_{battery} contribution in the system proves to be close to zero minor, despite the appreciable gradients in $n_e(r) = n_i(r)$ in the compressible plasma.

In Table III, we present key characterizing parameters for the system. The required bulk throughput power is given by the product of the total current and the voltage drop across the bulk plasma, and represents the power necessary to continue to drive the system in steady-state. Further in Table IV, we report a series of dimensionless numbers which help to characterize the plasma state and operating regime.

All other parameters of interest are presented in Table V, with values reported at the inner and outer radial positions since most of these parameters also vary across the annular space. Further, Table VI reports specifically on the calculated MFPs, collisional frequencies, and energy relaxation times. These comprehensive sets of plasma parameters are reported both to fully characterize the system, and to verify the self-consistency of the initial governing assumptions, commented on in the opening formulation (Sec. III A).

IV. PARAMETRIC STUDIES

In this section, each of the key input parameters is systematically varied within a physically reasonable range around the default condition values. The purpose of this parametric exploration is to investigate how variations in experimental input conditions influence the resulting steady-state plasma solutions. In addition to examining the core state variables—velocity, densities, and electric potential—we extend the analysis to include several derived quantities of practical interest. These include the total achieved compression ratio (using both the

TABLE IV. Dimensionless plasma parameters.

Quantity	Symbol	Value
Mach number (V_{peak})	M	3.02
Reynolds number (V_{peak})	Re	4.00×10^{3}
Magnetic Reynolds number (V_{peak})	Re_m	4.32×10^{-3}
Ratio of plasma pressure: magnetic pressure	β	1.80×10^{-2}
Ratio of atomic: molecular hydrogen	$\frac{n_H}{n_{H_2}}$	2.31×10^{9}

TABLE V. Plasma parameters of interest calculated at inner (R_1) and outer (R_2) radii.

Quantity	R_1	R_2
Neutral density n_n	$5.01 \times 10^{20}\ \mathrm{m}^{-3}$	$2.50 \times 10^{22}\ \mathrm{m}^{-3}$
Ion density n_i	$1.28 \times 10^{18}\ \mathrm{m}^{-3}$	$9.07 \times 10^{18}\ \mathrm{m}^{-3}$
Electron density n_e	$1.28 \times 10^{18}\ \mathrm{m}^{-3}$	$9.07 \times 10^{18}\ \mathrm{m}^{-3}$
Ionization fraction χ_i	2.56×10^{-3}	3.62×10^{-4}
Mass density ρ	$8.38 \times 10^{-7}\ \mathrm{kgm}^{-3}$	$4.19 \times 10^{-5}\ \mathrm{kgm}^{-3}$
Viscosity μ	6.11×10^{-6} Pas	6.11×10^{-6} Pas
Temperature $T_n = T_i = T_e$	5.80×10^{3} K	5.80×10^{3} K
Debye length λ_D	4.64×10^{-6} m	1.75×10^{-6} m
Sheath width $\sim 10\lambda_D$	4.64×10^{-5} m	1.75×10^{-5} m
Hydrodynamic boundary layer (BL) width δ_{BL}	4.63×10^{-2} m	1.35×10^{-2} m
Ion gyro radius ρ_i	3.30×10^{-4} m	3.30×10^{-4} m
Electron gyro radius ρ_e	7.69×10^{-6} m	7.69×10^{-6} m
Ion cyclo. frequency ω_{ci}	5.33×10^{6} Hz	5.33×10^{6} Hz
Electron cyclo. frequency ω_{ce}	9.79×10^{9} Hz	9.79×10^{9} Hz
Pedersen conductivity σ_P	$1.72 \times 10^{-1}\ \mathrm{Sm}^{-1}$	$3.49 \times 10^{-1}\ \mathrm{Sm}^{-1}$
Hall conductivity σ_H	$-5.55 \times 10^{-2}\ \mathrm{Sm}^{-1}$	$-4.13 \times 10\ \mathrm{Sm}^{-1}$
Electron thermal diffusivity	$2.72 \times 10^{3}\ \mathrm{m}^2\ \mathrm{s}^{-1}$	$5.43 \times 10^{1}\ \mathrm{m}^2\ \mathrm{s}^{-1}$
Electron conduction $t_{\mathrm{cond},e}$	2.36×10^{-7} s	1.18×10^{-5} s

TABLE VI. Mean free paths, collision frequencies, and energy relaxation times at R_1 and R_2.

Quantity	R_1	R_2
Mean free paths		
λ_{en}	1.72×10^{-2} m	3.44×10^{-4} m
λ_{in}	1.02×10^{-3} m	2.04×10^{-5} m
λ_{ee}	7.33×10^{-2} m	1.17×10^{-2} m
λ_{ei}	1.35×10^{2} m	2.16×10^{1} m
Collision frequencies		
ν_{en}	2.75×10^{7} Hz	1.37×10^{9} Hz
ν_{in}	1.08×10^{7} Hz	5.42×10^{8} Hz
ν_{ee}	6.46×10^{6} Hz	4.03×10^{7} Hz
ν_{ei}	3.51×10^{3} Hz	2.19×10^{4} Hz
Energy relaxation times		
$t_{en}^{(E)}$	3.34×10^{-5} s	6.68×10^{-7} s
$t_{in}^{(E)}$	9.23×10^{-8} s	1.85×10^{-9} s
$t_{ee}^{(E)}$	1.55×10^{-7} s	2.48×10^{-8} s
$t_{ei}^{(E)}$	2.61×10^{-1} s	4.19×10^{-2} s

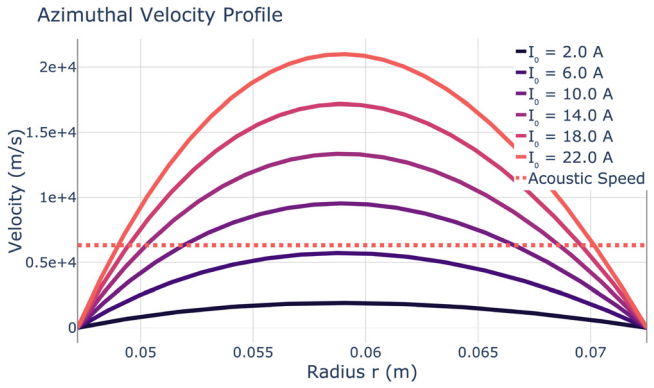

FIG. 8. Solution for the azimuthal velocity profile of the rotational plasma, compared with the acoustic speed through the plasma.

contrast and baseline-relative definitions) and the power throughput required to sustain the plasma through the bulk region. Together, these metrics provide insight into the operational sensitivity and performance characteristics of the system under varying conditions.

Regarding assumption verification: The study is conducted using a detailed parameter checking code which assesses the same set of plasma parameters reported in the tables of Sec. III C, as quantifiable metrics against the governing assumption conditions outlined in the formulation section. We strictly limit the parameter sweeps to the range of input variables where the outlined assumptions are assessed to PASS all checks in the accompanying sub-routine.

A. Parametric study: Variable input current I_0

Under the real laboratory experimental conditions, once a stable plasma has formed, a constant current is maintained in the range of 10–20 A. Therefore, for this parametric study, we explore the effect of linearly varying the applied current in the surrounding range of this known input current and explore the effect on the plasma condition.

The plot of azimuthal velocity in Fig. 8 shows that variation of input current produces a self-similar arcing profile, anchored to the no-slip boundary conditions, with peak velocities growing with approximately linear proportionality to I_0, which is logical from the solution equation for $u_\theta(r)$ by examination of the driving force term $\beta = \frac{I_0 B_z}{2\pi L \mu}$.

In Fig. 9, increasing the applied current I_0 shifts the density outward: the peak ion density at the outer wall R_2 rises slightly, while the inner-region density decreases (note that the log scale accentuates this visual change) relative to the baseline $n_i^{\mathrm{base}} = 5.73 \times 10^{18}\ \mathrm{m}^{-3}$. This behavior reflects a steady balance: stronger I_0 increases the $J_r \times B_z$ drive, raises u_θ, and hence enhances the centrifugal term $\sim u_\theta^2/r$, pushing mass outward and requiring rarefaction near R_1 for continuity. The profile steepening therefore tracks the centrifugal–hydrostatic balance; the additional transverse Lorentz contribution (direct radial force) associated with the Hall current (the $J_\theta B_z$ term) is found to be negligible as per the earlier analysis.

In Fig. 10, the total contrast compression ratio ($n_{\max}/n_{\min}$) increases approximately exponentially with input power, due to the rapid reduction in minimum density at the inner radius. In contrast, the baseline-relative compression ratio ($n_{\max}/n_{\mathrm{fill}}$) shows an initially steep increase followed by a degree of saturation, reflecting the finite number of particles available to accumulate at the outer edge. This

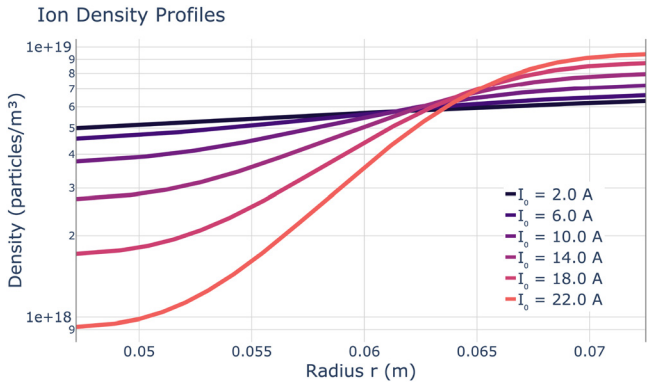

FIG. 9. Solution for plasma particle density profiles across the radial space.

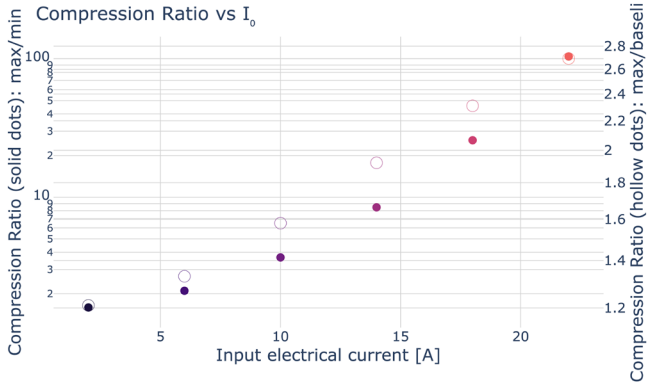

FIG. 10. Plot of compression ratios vs the varied input variable: n_{max}/n_{min} solid markers correspond to the left-side axis, and $n_{max}/n_{baseline}$ hollow markers to the right-side axis.

ceiling arises from the mass conservation constraint: as more particles are shifted outward, fewer remain to further increase peak density. Without an external mass inflow source, the achievable compression is fundamentally limited. If in-flow were permitted, this constraint would be relaxed, potentially enabling greater peak densities.

The relationship between particle density, conductivity, and the electric potential response in the plasma is more complex. Figure 11 shows the complicated response of the plasma to ion and neutral particle densities. When the Pederson conductivity drops in the inner region, the Ohmic term $\frac{C_0}{r\sigma_P(r)}$ in the integral for $\phi(r)$ gets amplified and drives a strong resistivity in the plasma, causing the electric potential to rise more quickly in this region, as seen for the high current case in Fig. 12. The corresponding response in required throughput power to drive the system is shown in Fig. 13.

B. Parametric study: Variable magnetic field strength B_z

The magnetic field strength in the experiment is limited by the capacity of the superconducting magnet, which has been run to a maximum of 0.35 T in the laboratory. Since this sets our physical limit, we

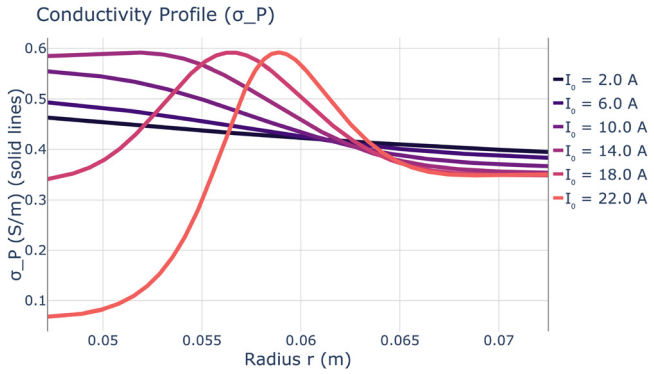

FIG. 11. Electric conductivity profiles across the annular space, in the steady state, for varying I_0 in the system.

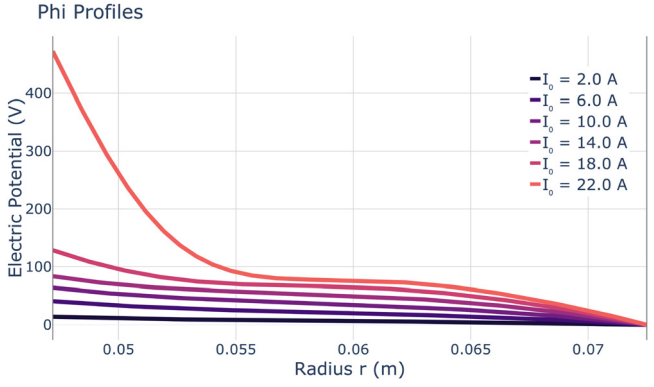

FIG. 12. Electric potential profile between the left anode and the grounded right side cathode.

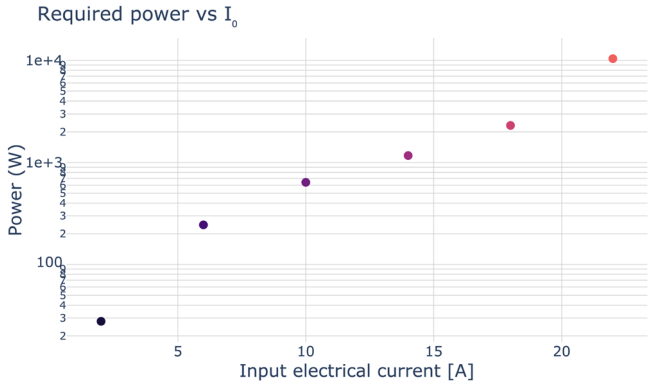

FIG. 13. Plot of bulk plasma throughput power required for steady-state operation vs the input variable.

explore a linear variation of B_z from $[0.1 : 0.35]$ T to study its effect on the plasma state condition.

Figures 14–16 show that varying the magnetic field strength in linear increments, the resulting plasma behavior appears reasonably congruent with that observed in the previous parametric study on

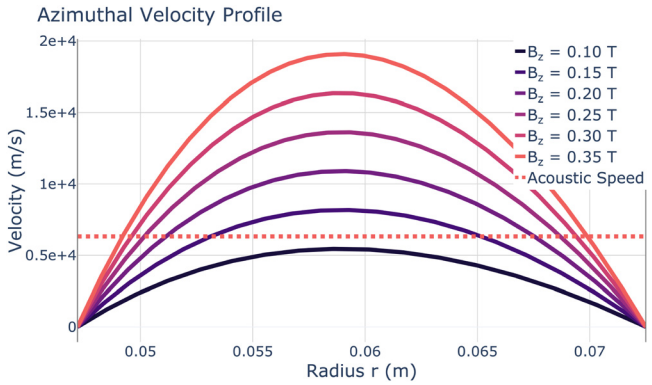

FIG. 14. Solution for the azimuthal velocity profile of the rotational plasma, compared with the acoustic speed through the plasma.

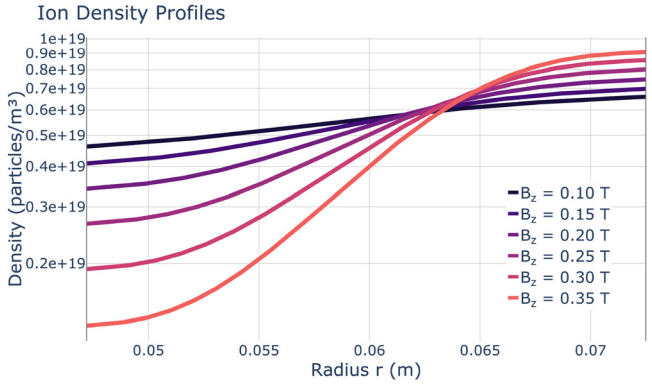

FIG. 15. Solution for plasma density profile across the radial space.

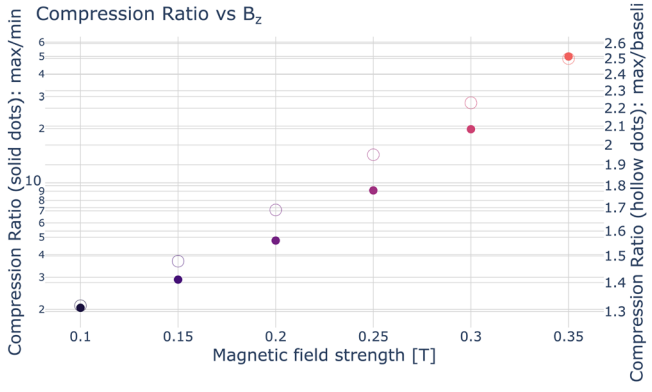

FIG. 16. Plot of compression ratios vs the varied input variable: n_{max}/n_{min} solid markers correspond to the left-side axis, and $n_{max}/n_{baseline}$ hollow markers to the right-side axis.

varying the input current. This congruence is naturally expected for the velocity profile when considering the u_θ equation driven by β, which encapsulates the product $I_0 B_z$ and governs the primary Lorentz forcing mechanism in the model. The observed symmetry in the

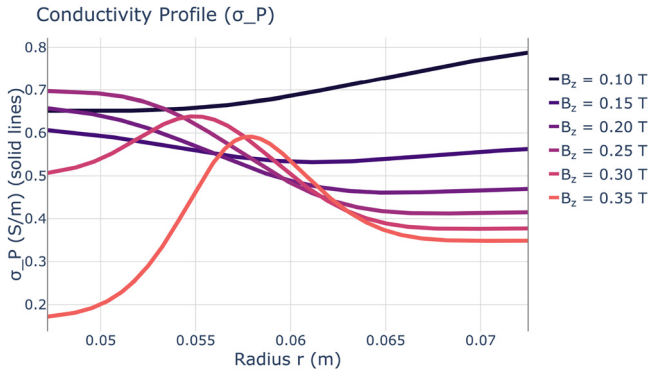

FIG. 17. Electric conductivity profiles across the annular space, in the steady state, for varying B_z in the system.

response of density from the current and magnetic field sweeps implies that the product of current and magnetic field in the Lorentz force—embedded explicitly within the β parameter—plays a leading-order role (via the induced centrifugal force $\propto u_\theta^2$) in setting the steady-state solution of ρ.

Again, the electrodynamic response in the system is more nuanced. While the solutions for u_θ and ρ were found mathematically to be independent of the electrical conductivity (term cancels in the analysis), the conductivity profile is important in determining the steady-state electric fields which form in response to the steady applied input current. In the parameter window under study, we see a significantly non-linear response in the Pederson conductivity (Fig. 17), which acts through the Ohmic term in the effective electric field, thereby influencing the response of the static electric potential $\phi(r)$ shown in Fig. 18. The corresponding oscillation and jump in the throughput power plot in Fig. 19 can be understood by looking closely at how ϕ intersects the inner R_1 axis and recalling that the throughput power is given by $I_0 \times \Delta\phi$.

Given the variation in throughput power, one could utilizing local minima as points where the compression ratio per unit power input is most favourable—suggesting conditions under which the plasma achieves maximal compressibility for minimal energetic cost. This

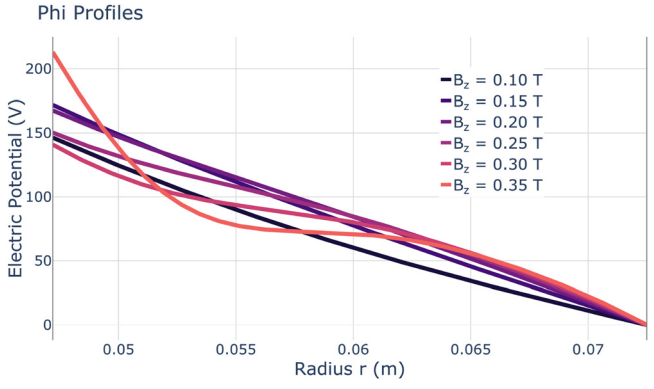

FIG. 18. Electric potential profile between the left anode and the grounded right side cathode.

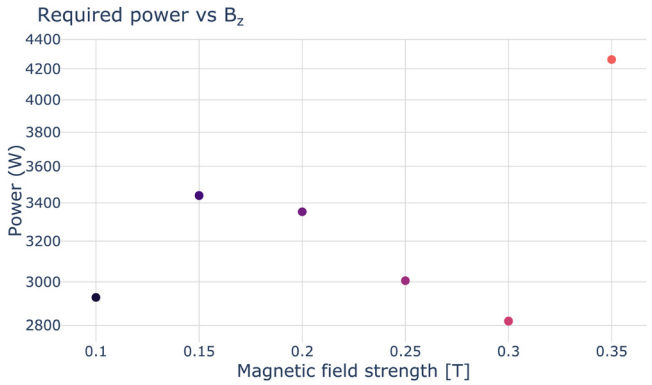

FIG. 19. Plot of bulk plasma throughput power required for steady-state operation vs the input variable: n_n.

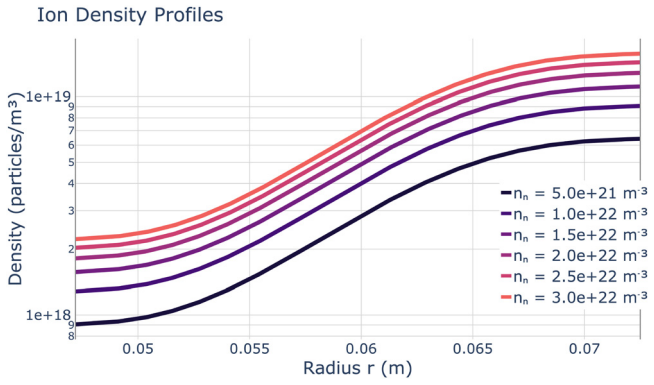

FIG. 20. Solution for plasma density profiles—both neutral and ion particle densities—across the radial space.

finding is particularly significant for the identification of operational optima for device design based on performance-to-power-efficiency criteria.

C. Parametric study: Variable plasma number density n_n

The neutral particle density, which approximates the total mass density in the weakly ionized regime, is treated as an input parameter, as it is back-calculated from the specified fill pressure in the experimental configuration. In this parametric study, we constrain the particle density to a range surrounding the default experimental condition, whereby we ensure the assumption checking sub-routine returns a `PASS` on all checks. Neutral density is varied linearly from 5×10^{21} to 3×10^{22} m^{-3} in this study.

We know from the derived governing steady-state equation that the u_θ solution is independent of density and conductivity, and therefore the azimuthal velocity profile exhibits insensitivity to changes in the initial fill pressure, and so the solution for all densities is given by the earlier default solution shown in Fig. 4(a).

It may seem counter-intuitive that the steady azimuthal velocity is insensitive to the neutral fill density, since spinning up a denser gas generally demands more torque. In our steady, current-driven model, the body torque is fixed by the imposed Lorentz force, and is balanced by viscous dissipation. For an ideal neutral gas, the dynamic viscosity $\mu = \mu(T)$ depends on temperature but not on density; with T taken uniform, μ is constant. So, in the steady-state equation for $u_\theta(r)$ depends on $(I_0, B_z, L, \mu(T))$ but, notably, not on n or σ_P. It is relevant to note that in a time-dependent spin-up problem, however, the ionization level χ_i and the Pedersen conductivity σ_P would directly influence the *time-scale* to reach steady state, rather than the steady velocity profile itself.

The density profiles in Fig. 20 retain a consistent radial shape across the range of fill pressures, but are vertically translated along the density axis. This behavior reflects the direct proportionality between fill pressure and total particle count throughout the domain, while preserving the shape of the compressive hydrostatic equilibrium and further implying a self-similar ionization fraction between density levels, whereby $n_i = \chi_i n_n$. Consistent with this result, the computed compression ratios—whether defined as total contrast or baseline-relative—therefore remain constant across the sweep of fill pressures.

Under the imposed current I_0, the Ohmic contribution to the radial field reads

$$E_r^{(\mathrm{Ohm})}(r) = -\frac{C_0}{r\,\sigma_P(r)}, \quad C_0 = \frac{I_0}{2\pi L},$$

so the net potential drop scales with a radial integral of $1/\sigma_P(r)$. The Pedersen conductivity $\sigma_P(n_n, r)$ is itself a strong, highly non-monotonic function of the neutral density n_n and radius as shown in Fig. 21. In our weakly ionized hydrogen plasma, $\nu_{en}, \nu_{in} \propto n_n$ while the magnetization parameters ω_{ce}/ν_{en} and ω_{ci}/ν_{in} decrease with n_n. At low n_n, σ_P increases with n_n; as n_n rises toward $\nu \sim \omega$, σ_P peaks; for still larger n_n, σ_P decreases approximately as $1/\nu(n_n)$. This highly non-monotonic behavior is further modulated by the Saha dependence of $n_e(r)$ on n_n. Consequently, $\Delta\phi(n_n)$ can exhibit pronounced nonlinear trends—including dips and rises—because $\Delta\phi \propto \langle 1/\sigma_P \rangle_r$. Within the parameter ranges explored here, the motional term $u_\theta B_z$ and the battery term $\frac{1}{n_e e}\frac{\partial p_e}{\partial r}$ remain subdominant to the Ohmic contribution, so the observed structure in $\Delta\phi(n_n)$ is primarily the reciprocal response to $\sigma_P(n_n, r)$.

The electric potential profiles are shown in Fig. 22, and the resultant throughput power scaling with fill density shown in Fig. 23.

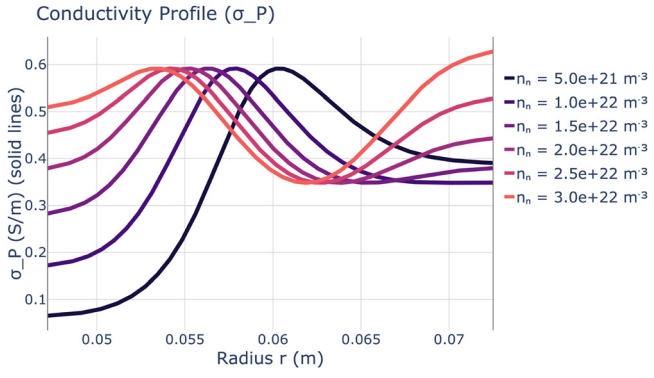

FIG. 21. Electric conductivity profiles across the annular space, in the steady state, for varying n_n in the system.

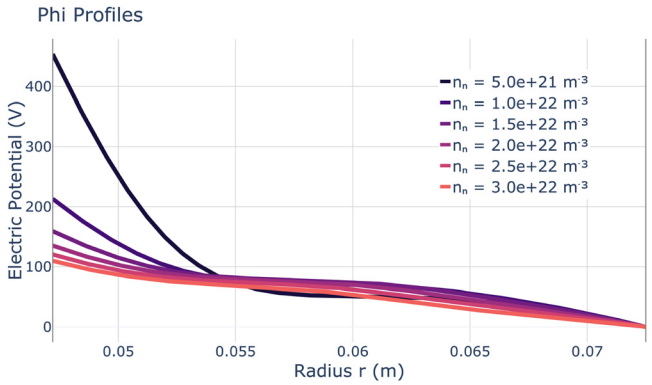

FIG. 22. Electric potential profile between the left anode and the grounded right side cathode.

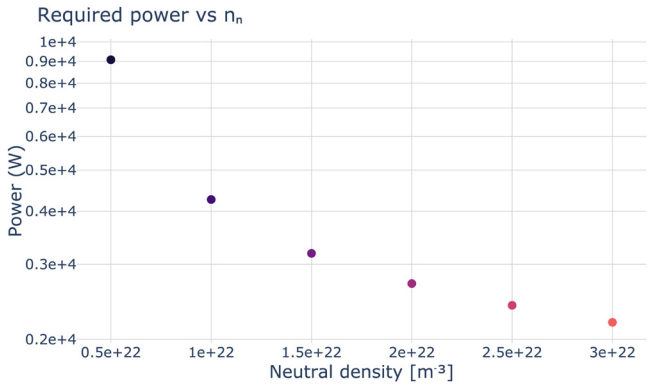

FIG. 23. Plot of bulk plasma throughput power required for steady-state operation vs the input variable: n_n.

V. CONCLUSIONS

This work developed a rigorous theoretical model describing the steady-state behavior of a centrifugally driven plasma within a novel experimental device. Plasma diagnostic systems are currently under development to support the experimental program, and future work will seek to validate the theoretical predictions through direct comparison with experimental measurements.

The cross-configuration of the Lorentz force-driven plasma means that very high velocities are predicted, especially in the central region of the annular space. The theoretical model predicts a highly supersonic regime. It should therefore be noted that while plasma particle compression is modest—by the definition of density rise above baseline—in the future case where the system introduces geometric obtrusions, one could expect to harness the presence of strong shockwaves, and their inherent high-density high-temperature post-shock stagnation regions. The modeling of such plasma conditions requires further advanced numerical modeling, incorporating explicit treatment of the energy equation and temporal evolution of the full fluid field.

Though mass separation was not the topic of this study, the steep sigmoidal density profiles computed under various input conditions demonstrate a potential for isotope separation applications. The performance of the coaxial configuration could be evaluated using this model against conventional plasma centrifuge configurations.

Several potential avenues for future device optimization and design improvements can be considered, along with possible extensions to additional applications, all of which must be grounded in a thorough understanding of the steady-state rotational plasma dynamics and the associated state characterization as developed in this model.

ACKNOWLEDGMENTS

I would like to thank and acknowledge M. Salazar and N. Abdalla for their insights into the experimental setup, P. Hsieh for coordinating laboratory operations, and J. P. Wang for comments on the manuscript.

The work of G. Gregori was performed under a contract from Oxford University Innovation.

AUTHOR DECLARATIONS

Conflict of Interest

Yes, Alpha Ring International Limited is a company that produces fusion-related technologies. The subject matter in this manuscript relates to a device intended for commercial purposes.

Author Contributions

H. A. Muir: Conceptualization (lead); Formal analysis (lead); Investigation (lead); Methodology (lead); Software (lead); Visualization (lead); Writing – original draft (lead); Writing – review & editing (lead). **N. Eschbach:** Data curation (supporting); Investigation (supporting); Methodology (supporting); Writing – original draft (supporting); Writing – review & editing (supporting). **G. Rodway-Gant:** Data curation (supporting); Investigation (supporting); Visualization (supporting); Methodology (supporting); Writing – original draft (supporting); Writing – review & editing (equal). **I. Vankov:** Investigation (supporting); Methodology (supporting); Project Administration (supporting); Writing – review & editing (equal). **A. Chen:** Formal analysis (supporting); Investigation (supporting); Methodology (supporting). **B. Wrixon:** Data curation (supporting); Formal analysis (supporting); Investigation (supporting); Software (supporting). **Z. Li:** Data curation (supporting); Project administration (lead); Resources (equal). **A. Gunn:** Conceptualization (supporting); Data curation (supporting); Methodology (supporting); Writing – review & editing (supporting). **G. Gregori:** Conceptualization (supporting); Investigation (supporting); Methodology (supporting); Supervision (lead); Writing – review & editing (lead).

DATA AVAILABILITY

The data and source code that support the findings of this study are available from the corresponding author upon reasonable request.

APPENDIX A: PARTITION FUNCTIONS IMPLEMENTED FOR SAHA DISSOCIATION MODEL

For atomic hydrogen, the partition function is given by

$$Q_{\mathrm{H}} = \sum_{n=1}^{\infty} g_n \exp\left(-\frac{E_n}{k_{\mathrm{B}}T}\right), \tag{A1}$$

where $g_n = 2n^2$ is the degeneracy of the n-th energy level, and $E_n = -13.6\,\mathrm{eV}/n^2$ is the corresponding energy of that level. Since we are concerned with the low-temperature regime, where $T \ll E_i$, only the ground state (i.e., $n = 1$) significantly contributes to the partition function. For example, at $T = 0.5\,\mathrm{eV}$, we have $E_1 = -13.6\,\mathrm{eV}$ and $g_1 = 2$, yielding the approximation $Q_{\mathrm{H}} \approx 2$.

For *diatomic hydrogen*, we must consider vibrational and rotational degrees of freedom in addition to the electronic partition function. The total partition function is thus expressed as

$$Q_{\mathrm{H}_2} = Q_e Q_v Q_r, \tag{A2}$$

where Q_e, Q_v, and Q_r denote the electronic, vibrational, and rotational partition functions, respectively. For molecular hydrogen, only a single spin state is populated at relevant temperatures, so the electronic partition function is $Q_e = 1$.

The energy of vibrational levels in a diatomic molecule is approximately given by

$$E_v = \hbar\omega_e\left(v + \frac{1}{2}\right), \tag{A3}$$

where $v = 0, 1, 2, \ldots$ is the vibrational quantum number, and $\hbar\omega_e$ is the characteristic vibrational energy. For molecular hydrogen, this vibrational quantum is approximately $\hbar\omega_e \approx 0.516\,\mathrm{eV}$.

The vibrational partition function is

$$Q_v = \sum_{v=0}^{\infty} \exp\left(-\frac{E_v}{k_{\mathrm{B}}T}\right). \tag{A4}$$

Using the geometric series approximation valid at low vibrational excitation, this becomes

$$Q_v \approx \frac{1}{1 - \exp\left(-\frac{\hbar\omega_e}{k_{\mathrm{B}}T}\right)}. \tag{A5}$$

Molecular hydrogen also exhibits quantized rotational energy levels. These are given by

$$E_J = BJ(J+1), \tag{A6}$$

where $J = 0, 1, 2, \ldots$ is the rotational quantum number, and B is the rotational constant. For H_2, the rotational constant is approximately $B \approx 60\,\mathrm{K} \approx 0.0052\,\mathrm{eV}$.

The rotational partition function is given by

$$Q_r = \sum_{J=0}^{\infty} (2J+1)\exp\left(-\frac{E_J}{k_{\mathrm{B}}T}\right). \tag{A7}$$

At high temperatures (or plasma conditions), where $k_{\mathrm{B}}T \gg B$, this sum can be approximated by the continuous expression

$$Q_r \approx \frac{k_{\mathrm{B}}T}{B}. \tag{A8}$$

APPENDIX B: EXPANSION OF INVISCID AND VISCOUS FLUXES IN THIS CYLINDRICAL SYSTEM

In this analysis, we mathematically expand the viscous and inviscid flux terms in the cylindrical coordinate system for a compressible flow. This involves applying the product rule and chain rule to express the fluxes explicitly in terms of their radial derivatives and cylindrical geometry.

Applying the product rule whereby

$$\frac{\partial}{\partial r}[rf(r)] = f(r) + r\frac{\partial f(r)}{\partial r}.$$

In this case, $f(r) = \rho u_r^2 + p$. Applying the product rule yields

$$\frac{1}{r}\cdot\frac{\partial}{\partial r}\left[r\left(\rho u_r^2 + p\right)\right] = \frac{1}{r}\cdot\left[\left(\rho u_r^2 + p\right) + r\frac{\partial}{\partial r}\left(\rho u_r^2 + p\right)\right].$$

Using the product rule expansions, the following expressions for the inviscid flux terms are obtained:

$$\frac{1}{r}\frac{\partial}{\partial r}(r\rho u_r) = \frac{\partial}{\partial r}(\rho u_r) + \frac{\rho u_r}{r},$$
$$\frac{1}{r}\frac{\partial}{\partial r}\left[r\left(\rho u_r^2 + p\right)\right] = \frac{\partial}{\partial r}\left(\rho u_r^2 + p\right) + \frac{\rho u_r^2}{r} + \frac{p}{r},$$
$$\frac{1}{r}\frac{\partial}{\partial r}(r\rho u_r u_\theta) = \frac{\partial}{\partial r}(\rho u_r u_\theta) + \frac{\rho u_r u_\theta}{r}.$$

The expansion of the viscous terms is more complex, but the resultant expansions are as follows.

r-momentum equation

$$(\nabla\cdot\boldsymbol{\tau})_r = \frac{1}{r}\frac{\partial}{\partial r}(r\,\tau_{rr}) - \frac{\tau_{\theta\theta}}{r}. \tag{B1}$$

With Stokes' hypothesis $\lambda = -\frac{2}{3}\mu$ and $\Theta = \frac{\partial u_r}{\partial r} + \frac{u_r}{r}$, the stress components become

$$\tau_{rr} = \frac{4}{3}\mu\frac{\partial u_r}{\partial r} - \frac{2}{3}\mu\frac{u_r}{r}, \quad \tau_{\theta\theta} = -\frac{2}{3}\mu\frac{\partial u_r}{\partial r} + \frac{4}{3}\mu\frac{u_r}{r}, \tag{B2}$$

$$\frac{1}{r}\frac{\partial}{\partial r}(r\,\tau_{rr}) = \frac{1}{r}\frac{\partial}{\partial r}\left[r\left(\frac{4}{3}\mu\frac{\partial u_r}{\partial r} - \frac{2}{3}\mu\frac{u_r}{r}\right)\right] = \frac{4}{3}\mu\frac{\partial^2 u_r}{\partial r^2} + \frac{2}{3}\mu\frac{1}{r}\frac{\partial u_r}{\partial r}, \tag{B3}$$

$$-\frac{\tau_{\theta\theta}}{r} = -\frac{1}{r}\left(-\frac{2}{3}\mu\frac{\partial u_r}{\partial r} + \frac{4}{3}\mu\frac{u_r}{r}\right) = \frac{2}{3}\mu\frac{1}{r}\frac{\partial u_r}{\partial r} - \frac{4}{3}\mu\frac{u_r}{r^2}, \tag{B4}$$

$$(\nabla\cdot\boldsymbol{\tau})_r = \frac{4}{3}\mu\left(\frac{\partial^2 u_r}{\partial r^2} + \frac{1}{r}\frac{\partial u_r}{\partial r} - \frac{u_r}{r^2}\right). \tag{B5}$$

θ-momentum equation

$$(\nabla\cdot\boldsymbol{\tau})_\theta = \frac{1}{r}\frac{\partial}{\partial r}(r\,\tau_{\theta r}) + \frac{\tau_{r\theta}}{r}. \tag{B6}$$

The axisymmetric shear component is

$$\tau_{\theta r} = \tau_{r\theta} = \mu\left(\frac{\partial u_\theta}{\partial r} - \frac{u_\theta}{r}\right). \tag{B7}$$

$$\frac{1}{r}\frac{\partial}{\partial r}(r\,\tau_{\theta r}) = \frac{\mu}{r}\frac{\partial}{\partial r}\left[r\left(\frac{\partial u_\theta}{\partial r} - \frac{u_\theta}{r}\right)\right] = \mu\frac{\partial^2 u_\theta}{\partial r^2}, \tag{B8}$$

$$\frac{\tau_{r\theta}}{r} = \mu\left(\frac{1}{r}\frac{\partial u_\theta}{\partial r} - \frac{u_\theta}{r^2}\right), \tag{B9}$$

$$(\nabla\cdot\boldsymbol{\tau})_\theta = \mu\left(\frac{\partial^2 u_\theta}{\partial r^2} + \frac{1}{r}\frac{\partial u_\theta}{\partial r} - \frac{u_\theta}{r^2}\right). \tag{B10}$$

APPENDIX C: SOLUTION OF THE AZIMUTHAL VELOCITY CONSTANTS UNDER NO-SLIP BOUNDARY CONDITIONS

Combining the homogeneous and particular solutions, the full solution for u_θ is

$$u_\theta(r) = D_1 r + \frac{D_2}{r} - \frac{1}{2}\beta r\ln(r),$$

where

$$\beta = \frac{I_0 B_z}{2\pi L\sigma_P\mu}.$$

The constants D_1 and D_2 can be determined from the boundary conditions by substituting R_1 and R_2 into the expressions and solving simultaneously

$$u_\theta(R_1) = D_1R_1 + \frac{D_2}{R_1} - \frac{\beta}{2}R_1\ln(R_1) = 0,$$
$$u_\theta(R_2) = D_1R_2 + \frac{D_2}{R_2} - \frac{\beta}{2}R_2\ln(R_2) = 0.$$

An expression for D_1 in terms of D_2 is obtained from the first boundary condition

$$D_1 = -\frac{D_2}{R_1^2} + \frac{\beta}{2}\ln(R_1).$$

Substituting this expression for D_1 into the second boundary condition $u_\theta(R_2) = 0$ yields

$$\frac{D_2R_2}{R_1^2} + \frac{\beta}{2}R_2\ln(R_1) + \frac{D_2}{R_2} - \frac{\beta}{2}R_2\ln(R_2) = 0.$$

Grouping terms involving D_2 and logarithmic terms gives

$$D_2 = \frac{\beta R_2^2R_1^2\ln\left(\frac{R_2}{R_1}\right)}{2\left(R_1^2 - R_2^2\right)},$$

and substituting this expression for D_2 back into D_1 gives

$$D_1 = \frac{\beta\left[R_2^2\ln(R_2) - R_1^2\ln(R_1)\right]}{2\left(R_1^2 - R_2^2\right)}.$$

Thus, the final expressions for the constants D_1 and D_2 are

$$D_1 = \frac{\beta\left[R_2^2\ln(R_2) - R_1^2\ln(R_1)\right]}{2\left(R_1^2 - R_2^2\right)},$$
$$D_2 = \frac{\beta R_2^2R_1^2\ln\left(\frac{R_2}{R_1}\right)}{2\left(R_1^2 - R_2^2\right)}.$$

APPENDIX D: INTERMEDIATE STEPS IN THE SOLUTION OF THE PLASMA DENSITY PROFILE

We solve for $\rho(r)$ where $u_\theta(r)$ is already determined. Returning to the governing steady-state system equation (*iii*) we then have

$$\frac{\partial\rho}{\partial r} = \frac{\rho u_\theta^2}{R_sTr} + \frac{\rho}{r} + \frac{\sigma_H}{\sigma_PR_sT}\cdot\frac{B_zI_0}{2\pi rL},$$

where we have established from the in-text analysis that the dominant solution is given by

$$\rho(r) = C_1\cdot e^{\int A(r)dr},$$

where C_1 is an integration constant, and $A(r)$ is given by

$$A(r) = \frac{1}{rR_sT}\cdot\left[D_1r + \frac{D_2}{r} - \frac{1}{2}\beta r\ln(r)\right]^2 + \frac{1}{r}.$$

The integral for $A(r)$ is cumbersome, and we must first conduct the term expansion before proceeding to solve its component integrals

$$\left[D_1r + \frac{D_2}{r} - \frac{1}{2}\beta r\ln(r)\right]^2 = \left[\frac{2D_1D_2}{r} + \frac{D_2^2}{r^3}D_1^2r - \left(D_1r + \frac{D_2}{r}\right)\cdot\beta\ln(r) + \frac{1}{4}\beta^2r\ln(r)\right]$$

$$\int A(r)\,dr = \frac{1}{R_sT}\cdot\left[\left(2D_1D_2 + \frac{1}{2}\beta D_1r^2 - \frac{1}{8}\beta^2r^2 + R_sT\right)\ln(r) + \left(\frac{1}{2}\beta D_2 + \frac{1}{8}\beta^2r^2\right)\ln^2(r) + \cdots + \left(-\frac{D_2^2}{2r^2} - \frac{1}{4}\beta D_1r^2 + \frac{1}{16}\beta^2r^2\right)\right] + C_2.$$

Substituting this result into the solution for $\rho(r)$, then rearranging and grouping of constant terms, we present the final solution as compactly as possible

$$e^{\int A(r)dr} = e^{C_2}\cdot e^{\frac{1}{R_sT}\left[\left(2D_1D_2 + \frac{1}{2}\beta D_1r^2 - \frac{1}{8}\beta^2r^2 + R_sT\right)\ln(r) + \left(\frac{1}{2}\beta D_2 + \frac{1}{8}\beta^2r^2\right)\ln^2(r) + \left(-\frac{D_2^2}{2r^2} - \frac{1}{4}\beta D_1r^2 + \frac{1}{16}\beta^2r^2\right)\right]},$$
$$\rho(r) = \rho_0\cdot r^{\left(\frac{2D_1D_2}{R_sT}+1\right)}\cdot e^{\frac{1}{R_sT}\left[\left(\frac{1}{2}\beta D_1r^2 - \frac{1}{8}\beta^2r^2\right)\ln(r) + \left(\frac{1}{2}\beta D_2 + \frac{1}{8}\beta^2r^2\right)\ln^2(r) + \left(-\frac{D_2^2}{2r^2} - \frac{1}{4}\beta D_1r^2 + \frac{1}{16}\beta^2r^2\right)\right]}. \tag{D1}$$

Here, ρ_0, a consolidation of the integration constants, is solved for by applying the condition that the total number of particles in the system must be conserved, as discussed in the text.

APPENDIX E: FULLY ANALYTICAL SOLUTION TO THE ELECTRIC POTENTIAL PROFILE UNDER CONSTANT χ_i σ_P ASSUMPTION

Considering the solution approach to electric potential

$$\phi(r) = \int \left[B_z u_\theta + \frac{m_i}{e}\left(\frac{u_\theta^2 + R_s T}{r} + R_s T \frac{\partial}{\partial r} \ln(\chi_i) \right) - \frac{C_0}{r\sigma_P} \right] dr, \quad \text{(E1)}$$

it is worth noting that in the case where electrical conductivity and ionization fraction were to be simplified and taken as constants (as it has been treated in other studies), then the term $\frac{\partial}{\partial r}\ln(\chi_i) = 0$, the term $-\frac{C_0}{r\sigma_P}$ is directly integrable, and a fully analytical solution is resolvable for the final equation for $\phi(r)$. We present this solution here:

Expanding the square of the velocity profile

$$\begin{aligned} u_\theta^2 &= \left(D_1 r + \frac{D_2}{r} - \frac{1}{2}\beta r \ln r \right)^2 \\ &= 2D_1 D_2 + \frac{D_2^2}{r^2} + D_1^2 r^2 - \left(D_1 r^2 + D_2 \right)\beta \ln r + \frac{1}{4}\beta^2 r^2 \ln^2 r, \end{aligned} \quad \text{(E2)}$$

the integrals are evaluated as

$$\int u_\theta(r)\, dr = \left(\frac{D_1}{2} + \frac{\beta}{8} \right) r^2 + \left(D_2 - \frac{\beta}{4} r^2 \right) \ln r + C, \quad \text{(E3)}$$

$$\begin{aligned} \int \frac{u_\theta^2}{r}\, dr = &\left(-\frac{1}{4}\beta D_1 + \frac{1}{16}\beta^2 \right) r^2 + \left(2D_1 D_2 + \frac{1}{2}\beta D_1 r^2 - \frac{1}{8}\beta^2 r^2 \right) \ln r \\ &+ \left(\frac{1}{2}\beta D_2 + \frac{1}{8}\beta^2 r^2 \right) \ln^2 r - \frac{D_2^2}{2r^2} + C, \end{aligned} \quad \text{(E4)}$$

$$\int \frac{C_0}{\sigma_P r}\, dr = \frac{E_0}{\sigma_P} \ln r + C, \quad \text{(E5)}$$

and one can obtain as the final solution for $\phi(r)$

$$\begin{aligned} \phi(r) = &\left[B_z \left(\frac{D_1}{2} + \frac{\beta}{8} \right) + \frac{m_i}{e}\left(-\frac{1}{4}\beta D_1 + \frac{1}{16}\beta^2 \right) \right] r^2 \\ &+ \left[B_z \left(D_2 - \frac{\beta}{4} r^2 \right) + \frac{m_i}{e}\left(2D_1 D_2 + \frac{1}{2}\beta D_1 r^2 \right.\right. \\ &\left.\left. - \frac{1}{8}\beta^2 r^2 + R_s T \right) - \frac{E_0}{\sigma_P} \right] \ln r \\ &+ \frac{m_i}{e}\left(\frac{1}{2}\beta D_2 + \frac{1}{8}\beta^2 r^2 \right) \ln^2 r - \frac{m_i}{e}\frac{D_2^2}{2r^2} + C. \end{aligned} \quad \text{(E6)}$$

REFERENCES

[1] A. Y. Wong, K. H. Lee, and L. C. Lee, "Simulation of dynamics of rotating weakly ionized plasmas," Phys. Plasmas **31**, 013101 (2024).
[2] H. E. Wilhelm and S. H. Hong, "Plasma rotation by electric and magnetic fields in a discharge cylinder," J. Appl. Phys. **48**, 561–567 (1977).
[3] M. M. B. Wijnakker, "Centrifugal effects in a weakly ionized rotating gas," Report No. INIS-mf–6327 (Amsterdam University, Netherlands, 1980).
[4] M. Y. Tanaka, "Vortex in plasma," Rev. Mod. Plasma Phys. **3**, 9 (2019).
[5] M. J. Hole and S. W. Simpson, "Performance of a vacuum arc centrifuge with a nonuniform magnetic field," Phys. Plasmas **4**, 3493–3500 (1997).
[6] A. J. Fetterman and N. J. Fisch, "Wave-driven countercurrent plasma centrifuge," Plasma Sources Sci. Technol. **18**(4), 045003 (2009).
[7] R. Gueroult, S. J. Zweben, N. J. Fisch, and J.-M. Rax, "E × B configurations for high-throughput plasma mass separation: An outlook on possibilities and challenges," Phys. Plasmas **26**, 043511 (2019).
[8] I. D. Kaganovich, A. Smolyakov, Y. Raitses, E. Ahedo, I. G. Mikellides, B. Jorns, F. Taccogna, R. Gueroult, S. Tsikata, A. Bourdon, J.-P. Boeuf, M. Keidar, A. T. Powis, M. Merino, M. Cappelli, K. Hara, J. A. Carlsson, N. J. Fisch, P. Chabert, I. Schweigert, T. Lafleur, K. Matyash, A. V. Khrabrov, R. W. Boswell, and A. Fruchtman, "Physics of E × B discharges relevant to plasma propulsion and similar technologies," Phys. Plasmas **27**, 120601 (2020).
[9] J.-P. Boeuf and A. Smolyakov, "Physics and instabilities of low-temperature E × B plasmas for spacecraft propulsion and other applications," Phys. Plasmas **30**, 050901 (2023).
[10] M. M. B. Wijnakker, E. H. A. Granneman, and J. Kistemaker, "A study of a weakly ionized rotating plasma," J. Phys. Colloq. **40**(C7), C7-487–C7-488 (1979).
[11] M. M. B. Wijnakker and E. H. A. Granneman, "Limitations on mass separation by the weakly ionized plasma centrifuge," Z. Naturforsch., A: Phys. Sci. **35**, 883–893 (1980).
[12] B. Lehnert, "The partially ionized plasma centrifuge," Phys. Scr. **7**, 102 (1973).
[13] R. Gueroult, D. T. Hobbs, and N. J. Fisch, "Plasma filtering techniques for nuclear waste remediation," J. Hazard. Mater. **297**, 153–159 (2015).
[14] R. Gueroult, J.-M. Rax, and N. J. Fisch, "Opportunities for plasma separation techniques in rare earth elements recycling," J. Cleaner Prod. **182**, 1060–1069 (2018).
[15] D. Baker and J. Hammel, "Rotating plasma experiments. II. Energy measurements and the velocity limiting effect," Phys. Fluids **4**, 1549–1558 (1961).
[16] V. Volosov, "MHD stability of a hot rotating plasma: A brief review of PSP-2 experiments," Plasma Phys. Rep. **35**, 719–733 (2009).
[17] R. Ellis, A. Hassam, S. Messer, and B. Osborn, "An experiment to test centrifugal confinement for fusion," Phys. Plasmas **8**, 2057–2065 (2001).
[18] N. R. Schwartz, I. G. Abel, A. B. Hassam, M. Kelly, and C. A. Romero-Talamás, "Mctrans++: A 0-D model for centrifugal mirrors," J. Plasma Phys. **90**, 905900217 (2024).
[19] M. Krishnan, M. Geva, and J. Hirshfield, "Plasma centrifuge," Phys. Rev. Lett. **46**, 36 (1981).
[20] B. James and S. Simpson, "Isotope separation in the plasma centrifuge," Plasma Phys. **18**, 289 (1976).
[21] O. A. Anderson, W. R. Baker, A. Bratenahl, J. J. Ise, W. B. Kunkel, J. M. Stone, and H. P. Furth, "Hydromagnetic capacitor," in *Proceedings of the United Nations International Conference on the Peaceful Uses of Atomic Energy* (United Nations, Geneva, Switzerland, 1958), pp. 155–160.
[22] P. Barber, D. Swift, and B. Tozer, "The formation of rotating plasmas in a homopolar configuration," J. Phys. D: Appl. Phys. **5**, 693 (1972).
[23] S. Simpson, P. Seebacher, and H. Messerle, "Study of a continuous plasma centrifuge," J. Phys. D: Appl. Phys. **20**, 622 (1987).
[24] A. Y. Wong and C.-C. Shih, "Enhancement of nuclear fusion in plasma oscillation systems," Plasma **5**, 176–183 (2022).
[25] B. P. Pandey, J. Vranjes, and S. V. Vladimirov, "The stability of weakly ionized collisional dusty plasma in the presence of flow," Phys. Plasmas **19**, 093701 (2012).
[26] J. Allen, "The plasma-sheath boundary: Its history and Langmuir's definition of the sheath edge," Plasma Sources Sci. Technol. **18**, 014004 (2009).
[27] V. A. Shakhatov and Y. A. Lebedev, "Collisional-radiative model of hydrogen low-temperature plasma: Processes and cross sections of electron-molecule collisions," High Temp. **49**, 257–302 (2011).
[28] W. A. Stygar, G. A. Gerdin, and D. L. Fehl, "Analytic electrical-conductivity tensor of a nondegenerate Lorentz plasma," Phys. Rev. E **66**, 046417 (2002).
[29] D. Meral "LIII. Ionization in the solar chromosphere," Lond. Edinb. Dublin Philos. Mag. J. Sci. **40**(238), 472–488 (1920).
[30] J.-S. Yoon, M.-Y. Song, J.-M. Han, S. H. Hwang, W.-S. Chang, B. Lee, and Y. Itikawa, "Cross sections for electron collisions with hydrogen molecules," J. Phys. Chem. Ref. Data **37**, 913–931 (2008).
[31] J. Vranjes and P. S. Krstic, "Collisions, magnetization, and transport coefficients in the lower solar atmosphere," Astron. Astrophys. **554**, A22 (2013).